Chemistry, mineralogy, and grain properties at Namib and High dunes, Bagnold dune field, Gale crater, Mars: A synthesis of Curiosity rover observations

B. L. Ehlmann, K. S. Edgett, B. Sutter, C. N. Achilles, M. L. Litvak, M. G. A. Lapotre, R. Sullivan, A. A. Fraeman, R. E. Arvidson, D. F. Blake, et al.

HAL Id: insu-03676799
https://insu.hal.science/insu-03676799

RESEARCH ARTICLE

Key Points:
- Because of ongoing aeolian activity, the Bagnold dunes consist of well-sorted sands and lack the finer grains typical of Martian soils
- Dune sands are chemically distinct with elevated Si, Mg, and Ni and lower H_2O, S, and Cl relative to all previously measured Martian fines
- Two distinct, water-/OH-bearing amorphous components are identified: Fe-, S-, and Cl-rich material in dust and Si-rich material in the sands

Correspondence to:
B. L. Ehlmann,
ehlmann@caltech.edu

Chemistry, mineralogy, and grain properties at Namib and High dunes, Bagnold dune field, Gale crater, Mars: A synthesis of Curiosity rover observations

B. L. Ehlmann[1,2] iD, K. S. Edgett[3] iD, B. Sutter[4,5] iD, C. N. Achilles[6] iD, M. L. Litvak[7], M. G. A. Lapotre[1], R. Sullivan[8], A. A. Fraeman[2] iD, R. E. Arvidson[9] iD, D. F. Blake[10] iD, N. T. Bridges[11,12] iD, P. G. Conrad[13], A. Cousin[14] iD, R. T. Downs[6], T. S. J. Gabriel[15] iD, R. Gellert[16] iD, V. E. Hamilton[17] iD, C. Hardgrove[15], J. R. Johnson[11] iD, S. Kuhn[2], P. R. Mahaffy[13] iD, S. Maurice[14,18], M. McHenry[2], P.-Y. Meslin[14] iD, D. W. Ming[5] iD, M. E. Minitti[11] iD, J. M. Morookian[2], R. V. Morris[5], C. D. O'Connell-Cooper[19] iD, P. C. Pinet[14,18], S. K. Rowland[20], S. Schröder[21,22] iD, K. L. Siebach[23] iD, N. T. Stein[1] iD, L. M. Thompson[18] iD, D. T. Vaniman[24] iD, A. R. Vasavada[2] iD, D. F. Wellington[14,15], R. C. Wiens[25] iD, and A. S. Yen[2]

[1]Division of Geological and Planetary Sciences, California Institute of Technology, Pasadena, California, USA, [2]Jet Propulsion Laboratory, California Institute of Technology, Pasadena, California, USA, [3]Malin Space Science Systems, San Diego, California, USA, [4]Jacobs Technology, Houston, Texas, USA, [5]NASA Johnson Space Center, Houston, Texas, USA, [6]Department of Geosciences, University of Arizona, Tucson, Arizona, USA, [7]Space Research Institute—RAS, Moscow, Russia, [8]Cornell Center for Astrophysics and Planetary Science, Cornell University, Ithaca, New York, USA, [9]Department of Earth and Planetary Sciences, Washington University in Saint Louis, Saint Louis, Missouri, USA, [10]Exobiology Branch, NASA Ames Research Center, Moffett Field, California, USA, [11]Johns Hopkins University Applied Physics Laboratory, Laurel, Maryland, USA, [12]Deceased 26 April 2017, [13]NASA Goddard Space Flight Center, Greenbelt, Maryland, USA, [14]Institut de Recherche en Astrophysique et Planétologie, CNRS-Université Toulouse, Toulouse, France, [15]School of Earth and Space Exploration, Arizona State University, Tempe, Arizona, USA, [16]Guelph-Waterloo Physics Institute, University of Guelph, Guelph, Ontario, Canada, [17]Department of Space Studies, Southwest Research Institute, Boulder, Colorado, USA, [18]Observatoire Midi-Pyrénées, Université de Toulouse, Toulouse, France, [19]Planetary and Space Science Centre, University of New Brunswick, Fredericton, New Brunswick, Canada, [20]Department of Geology and Geophysics, University of Hawai'i at Mānoa, Honolulu, Hawaii, USA, [21]Institut de Recherche en Astrophysique et Planétologie, Toulouse, France, [22]Institut für Optische Sensorsysteme, German Aerospace Center (DLR), Berlin, Germany, [23]Department of Geosciences, Stony Brook University, Stony Brook, New York, USA, [24]Planetary Science Institute, Tucson, Arizona, USA, [25]Los Alamos National Laboratory, Los Alamos, New Mexico, USA

Abstract The Mars Science Laboratory Curiosity rover performed coordinated measurements to examine the textures and compositions of aeolian sands in the active Bagnold dune field. The Bagnold sands are rounded to subrounded, very fine to medium sized (~45–500 μm) with ≥6 distinct grain colors. In contrast to sands examined by Curiosity in a dust-covered, inactive bedform called Rocknest and soils at other landing sites, Bagnold sands are darker, less red, better sorted, have fewer silt-sized or smaller grains, and show no evidence for cohesion. Nevertheless, Bagnold mineralogy and Rocknest mineralogy are similar with plagioclase, olivine, and pyroxenes in similar proportions comprising >90% of crystalline phases, along with a substantial amorphous component (35% ± 15%). Yet Bagnold and Rocknest bulk chemistry differ. Bagnold sands are Si enriched relative to other soils at Gale crater, and H_2O, S, and Cl are lower relative to all previously measured Martian soils and most Gale crater rocks. Mg, Ni, Fe, and Mn are enriched in the coarse-sieved fraction of Bagnold sands, corroborated by visible/near-infrared spectra that suggest enrichment of olivine. Collectively, patterns in major element chemistry and volatile release data indicate two distinctive volatile reservoirs in Martian soils: (1) amorphous components in the sand-sized fraction (represented by Bagnold) that are Si-enriched, hydroxylated alteration products and/or H_2O- or OH-bearing impact or volcanic glasses and (2) amorphous components in the fine fraction (<40 μm; represented by Rocknest and other bright soils) that are Fe, S, and Cl enriched with low Si and adsorbed and structural H_2O.

Plain Language Summary The Bagnold dune field is an active sand field with moving dunes and sits between the landing site of the Curiosity rover and rocks of interest higher up on Mount Sharp. When passing through the dune field, we used all of Curiosity's instruments to measure the chemistry, mineralogy, and grain size of sands in the Bagnold dune field in order to figure out where they came from, how the sands are transported, and what volatile materials (like water) lie within Martian soils. We found that the Bagnold

sand dunes are very well sorted; no dusty materials are found within them, in stark contrast to soils seen previously with Curiosity and with rovers at other landing sites. We found that the coarser sand grains are enriched in the volcanic minerals olivine and pyroxene, confirming a prediction from orbit that wind-related activity seems to concentrate these phases. We also found that the dunes were much lower in water and other volatile elements like sulfur and chlorine versus all previous Mars soils. Using a combination of the rover's sieving system and chemical measurement tools, we figured out that two types of materials host water. In the first type of material, common in these sands, water is low in abundance (≤~1%), very tightly bound to the grains, and is not released until temperatures >200°C. In the second type of material, water is higher in abundance (2%) and more easily released by heating. Sieved water-bearing fine materials may be a useful resource for human explorers.

1. Introduction

Aeolian processes currently dominate the modification of Martian landscapes today. Evidence for the longevity of wind-driven processes is recorded in ancient (>3 Ga) cross-bedded aeolian sandstones, which serve as indicators for past climate, wind direction, and atmospheric pressure [e.g., *Edgett and Malin*, 2000; *Grotzinger et al.*, 2005; *Milliken et al.*, 2014; *Lapotre et al.*, 2016; *Banham et al.*, 2016]. Extensive dunes (designated informally as the Bagnold dune field) lie across the intended long-range traverse of the Mars Science Laboratory rover, Curiosity. These dunes provided a unique opportunity to study an active Martian aeolian system to examine the physics of sand transport on Mars, the chemistry and mineralogy of Martian aeolian sands, their relationship to nearby rock types, and the mixing, sorting, and abrasion that results from wind transport [*Bridges and Ehlmann*, 2017]. The Bagnold dunes are located along a topographic break in slope on the lower northwest flank of Aeolis Mons (informally named Mount Sharp) (Figure 1). The dunes extend ~30 km northeast to southwest, spanning 1–2 km in width in the vicinity of the Mars Science Laboratory (MSL) traverse. The dunes migrate at a rate of ~0.4 m per Earth year, driven by winds predominantly from the northeast [e.g., *Silvestro et al.*, 2013; *Bridges et al.*, 2014; *Newman et al.*, 2017]. The dune field hosts a range of morphologies, including barchans near the northern and western margins of the field and longitudinal dunes in the central portions [e.g., *Hobbs et al.*, 2010]. Numerous sand-filled hollows are also located in and around the active field, likely due to trapping of sands within impact craters and other depressions.

As on Earth, sand-sized grains (62.5 μm to 2 mm) on Mars can be mineral grains, lithic fragments, or amorphous particles generated by weathering and erosion of rock (epiclasts) or produced by explosive volcanism (tephragenic clasts). Direct arrival of sand-size meteoritic input, impact event-generated clasts (impactogenic clasts), and aggregates of silt- and clay-sized fines are additional potential sources. Sand deposits are not only indicators of particle production, they are also records of clast segregation by sorting, transport, and deposition by a fluid (e.g., water and wind). On Earth, aeolian dune sands are typically a wind-sorted, reworked product of previously water-transported sands. Sand liberated from previous sand-bearing sedimentary rocks can also be reworked into dunes (e.g., Coral Pink dunes in Utah, USA [*Gregory*, 1950]), but dune sand can also be created from mechanical breakdown of igneous or metamorphic rock (e.g., Moses Lake dunes in Washington, USA, [*Petrone*, 1970; *Bandfield et al.*, 2002]).

Windblown Martian sand is dominated by basaltic materials [e.g., *Yen et al.*, 2005; *Rogers and Aharonson*, 2008; *Tirsch et al.*, 2011; *Pan and Rogers*, 2017] reflecting the dominant composition of that planet's crust [e.g., *Rogers and Christensen*, 2007; *McSween et al.*, 2010; *McLennan*, 2012]. This is somewhat similar to Earth, except that on our planet the silicic continental crust that serves as the source for most sands is dominated by feldspars, which chemically weather into clay minerals and small particles that are not efficiently transported by saltation. Therefore, most terrestrial dunes consist of a residual quartz-rich fraction that is resistant to weathering. With a lack of significant hydrous and other chemical weathering processes on Mars, dune sands offer a less altered petrologic window into source rock composition(s) and sediment sorting processes.

Spectroscopic data acquired by instruments aboard orbiting spacecraft show that the Bagnold dunes appear to be enriched in mafic minerals relative to materials in the surrounding Bradbury and Mount Sharp group rocks. This contrast may result from inherent differences in mineralogy that reflect contributions from rocks over a broader geographic area, differences in grain size and texture (e.g., coarser grains causing stronger spectral features), lack of dust cover on dunes relative to the rocks due to aeolian activity, or some combination of these factors. Thermal infrared spectroscopic data ranging from 100 m/pixel to ~3 km/pixel indicate
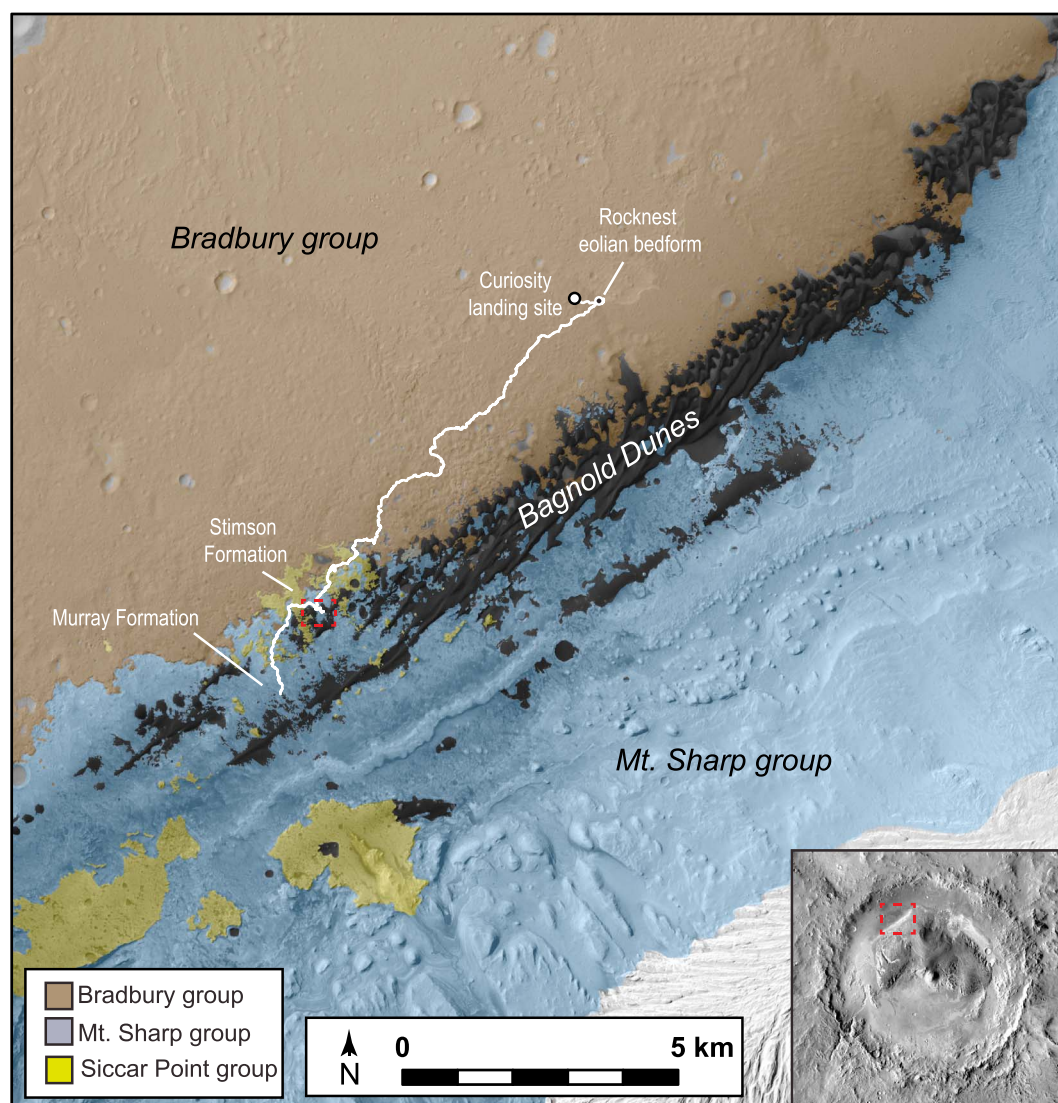
Figure 1. Overview of the study area, showing the Bagnold dune field, rover traverse through sol 1550, and key rock units: the Bradbury group (Aeolis Palus) with its interbedded sandstones, the Siccar Point group (including the Stimson sandstone formation), and the Mount Sharp group (including the Murray formation). Geologic mapping is from *Grotzinger et al.* [2015] and *Fraeman et al.* [2016] on a Mars Reconnaissance Orbiter Context Camera image basemap. The dashed red box shows the location at which the Bagnold dunes campaign was conducted and is the approximate location of Figure 2. The inset shows the location of this scene within Gale crater.

that the Bagnold dunes are olivine basaltic in composition [*Rogers and Bandfield*, 2009] with the olivine composition modeled to be ~$Fo_{55\pm5}$ [*Lane and Christensen*, 2013]. Visible/shortwave infrared imaging spectrometer data at ~20 m/pixel resolution show that the distribution of mafic minerals is not homogenous. Variations in absorption band strengths of olivine and pyroxene are observed when comparing barchan dunes on the outer margins of the field with longitudinal dunes in the central portions of the field [*Seelos et al.*, 2014; *Lapotre et al.*, 2017].

Thus, the Bagnold dunes present an opportunity to study aeolian sedimentary sorting, mineral segregation, and consequent changes in bulk chemistry with erosion and transport, as well as to ground truth remote sensing data. This is significant for multiple reasons. First, an overall question in Mars geology is the origin and transport history of present-day, loose, fine-grained materials at the Martian surface, which we refer to as soils per the "engineering sense" described by *Knox* [1968] (grains of clay, silt, sand, and granule size). Few micrometer-sized, wind-blown dust is transported globally, but to what extent are soils globally homogenized? Does saltation over long geologic time and distance coupled with meteoritic impact processes lead

to similar soils globally or do compositional similarities between sites merely represent the chemical similarity of different parent basaltic lithologies, averaged over a local area? Data from Gale crater can be compared to chemical and mineralogical data of soils at other landing sites to understand the nature of soil production and aeolian transport processes.

Second, understanding present-day aeolian processes is a key to interpreting the past. For Gale crater specifically, the question of sedimentary sources and sinks is relevant for understanding its sedimentary rocks and the provenance of clastic materials in the bedrock formations explored by Curiosity. This is a major issue raised by the analyses of sedimentary rock units in Gale so far because of compositional diversity, including basaltic and nonbasaltic lithologies. Conglomerates in the Bradbury group of Aeolis Palus include high-alkali rocks and cobbles of feldspathic materials [e.g., *Stolper et al.*, 2013; *Sautter et al.*, 2014; *Schmidt et al.*, 2014; *Mangold et al.*, 2016], inferred to derive from the crater walls and rim. Yellowknife Bay clay mineral-bearing mudstones (Bradbury group) and the Rocknest aeolian bedform have basaltic bulk chemical compositions, which are similar for major elements, but different mineralogies, which are inferred to result from the quasi-isochemical alteration of olivine to form saponite and magnetite [*McLennan et al.*, 2014; *Vaniman et al.*, 2014; *Bristow et al.*, 2015]. A comprehensive study of the chemistry of all Bradbury group target rocks shows that grain size segregation of basaltic and felsic minerals during breakdown and transport of a sub-alkaline plagioclase-phyric basalt explains much (but not all) of their observed compositional diversity [*Siebach et al.*, 2017]. However, one set of sandstones at the Kimberley investigation site (Bradbury group) is distinct, significantly enriched in potassium [*Le Deit et al.*, 2016; *Thompson et al.*, 2016]; as such, a different source region and parent rock has been invoked [*Treiman et al.*, 2016].

Separating differences in sedimentary rocks resulting from weathering and diagenesis (signifying past waters long lived enough to cause chemical change) versus transport and sorting is thus vital to interpreting the environmental history recorded in the sedimentary rocks within Gale crater. These distinctions are particularly important given the presence of aeolian and fluvial sandstones interbedded with or overlying lacustrine units [*Grotzinger et al.*, 2014, 2015; *Banham et al.*, 2017; *Edgar et al.*, 2017] and cross-bedded sandstones that lie ahead in Mount Sharp [*Milliken et al.*, 2014]. Investigation of the composition and textural diversity of the Bagnold dune sands allows us to investigate basaltic sedimentary materials without complications of diagenetic overprinting. An assumption sometimes made is that the soils of Gale crater represent a protolith for the sedimentary rocks of Mount Sharp, a hypothesis that will be examined here.

Third, prior work using data acquired by instruments on orbiting spacecraft shows regions mantled with fine-grained materials have enhanced hydration [e.g., *Houck et al.*, 1973; *Bibring et al.*, 1989; *Feldman et al.*, 2004; *Ruff*, 2004; *Jouglet et al.*, 2007; *Milliken et al.*, 2007; *Audouard et al.*, 2014]. In situ data show that Martian soils contain at least 1% water and sometimes a few percent more [e.g., *Anderson and Tice*, 1979; *Smith et al.*, 2009; *Leshin et al.*, 2013]. Thus, how much water and other volatiles are stored in Martian soils and their form is important for understanding modern and ancient cycling of volatiles. It is also relevant to characterizing resources that could be available to support human exploration.

In this paper, we synthesize the results derived from Curiosity's observations of the chemistry, mineralogy, color, grain size, and textures of the dune sands investigated during our first Bagnold campaign to address these issues. This overview focuses on (1) comparison of the chemistry of the Bagnold dune sands to other fines across Mars and sedimentary rocks in Gale crater, (2) assessment of the degree to which physical sorting results in compositional change and heterogeneity in bulk sand composition, and (3) the assessment of the volatile (H, C, N, O, and S) content of the sands relative to other materials examined by landed missions. After briefly describing the methodology of the Bagnold campaign and instruments employed, we report the chemistry, mineralogy, and spectroscopic properties of the dunes, comparing to other data sets and addressing the issues above.

2. Instruments and Data Sets

2.1. Measurement Locations, Strategy, and Sample Processing

Further details of all rover activities as part of the Bagnold dunes campaign are given in *Bridges and Ehlmann* [2017]. In brief, the rover visited the margins of two barchan dunes (High dune and Namib dune), situated at the northern trailing edge of the dune field, for compositional and textural studies (Figure 2). Driving on the dunes with all rover wheels was precluded by vehicle safety considerations, so the choice of sites was
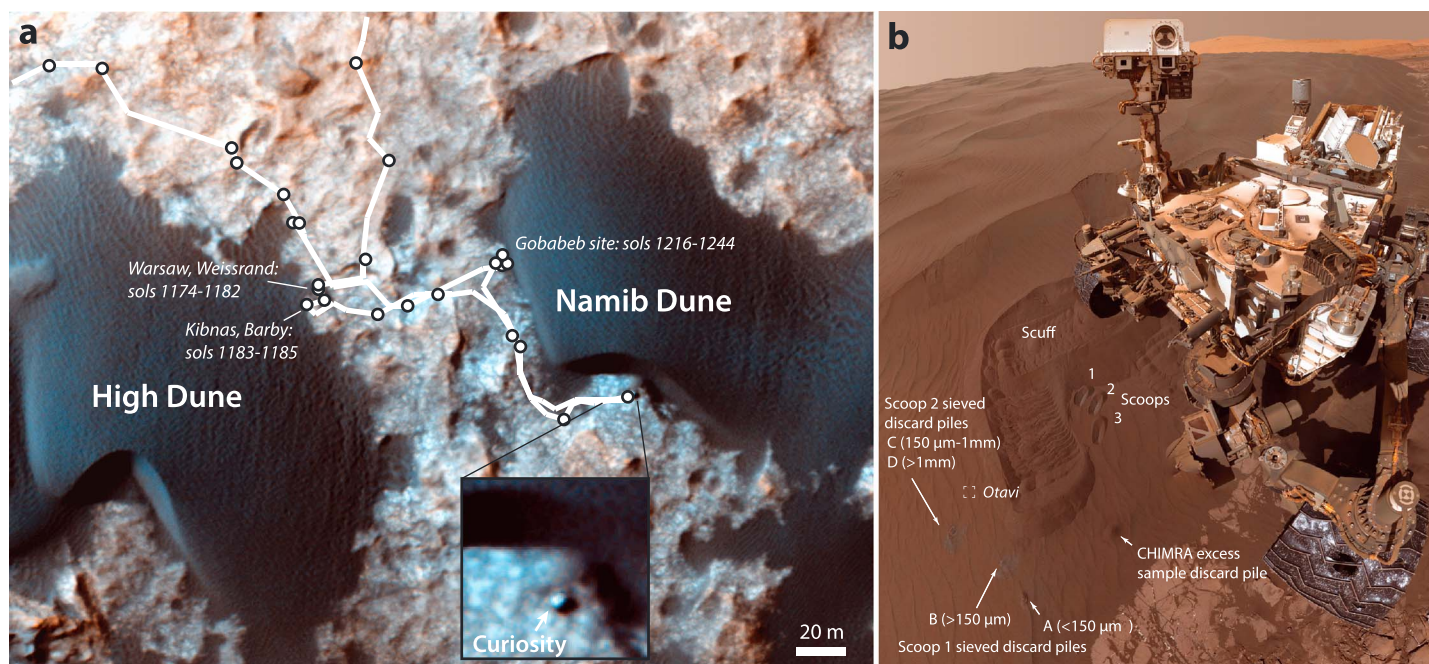
Figure 2. Overview of measurement and sampling locations for the Bagnold dune campaign. (a) A stretched red, green, blue simulated true color image from HiRISE ESP_044172_1755, indicating the rover path and locations of in situ study at Namib and High Dunes. The image was acquired on Curiosity sol 1207 with the rover next to Namib dune. The inset shows the Curiosity rover at the lee face of Namib dune. (b) The Gobabeb locality at Namib dune where dune sands were disrupted by a wheel scuff, scooped, sieved, and discarded for a coordinated suite of measurements with the rover compositional instruments. This is a mosaic of MAHLI images acquired on sols 1228 and 1241. The rover wheel width is approximately 40 cm, and the scoop widths are approximately 4 cm; the robotic arm is not visible because the camera, which acquired the mosaic, is on the arm.

dictated by a combination of rover accessibility, operational constraints for time efficiency (i.e., study areas located not too far from the MSL team's strategic traverse route for investigating Mount Sharp rock units), and science merit. The initial part of the measurement campaign was opportunistic and occurred upwind and adjacent to High dune in a sand patch in which soil mechanics experiments and traversability tests were conducted (Martian solar days (sol) 1182) and on the edge of the stoss of High dune (sol 1184). Remote and contact science measurements were acquired on natural and rover-disturbed targets (Figures 2a and 3).

Most of the campaign was conducted at a site named Gobabeb, located on the western secondary lee face of Namib dune (sols 1216–1244). The site was chosen because of evidence for relatively high activity (compared to other accessible parts of the dune field) observed in time series of high-resolution images acquired from orbit, showing ripple migration rates of up to ~1.7 m/Earth year [*Silvestro et al.*, 2016; *Bridges et al.*, 2017; *Lapotre et al.*, 2017]. Visible and near-infrared spectral data also showed low dust cover and possible enrichment of olivine, two parameters correlated with dune activity [*Lapotre et al.*, 2017].

At the Gobabeb site along the margin of Namib dune (Figure 2), the rover acquired a coordinated set of observations using all payload instruments, including the sample acquisition and processing subsystem to segregate dune sand by grain size (Table 1). We also performed active neutron spectroscopy upon ingress and egress to the site. Upon arrival at the dune, Curiosity was commanded to "scuff" the dune, an activity in which the right-front rover wheel was rotated 90° within the sand to disrupt it and enable measurement of both surface and interior dune sands (Figure 2b) [e.g., *Sullivan et al.*, 2011].

Three scoops of material were extracted at Gobabeb and processed with the rover sample handling system (described by *Anderson et al.* [2012]) to obtain size separates with grain sizes of <150 μm (samples A and E), >150 μm (samples B and F), 150 μm to 1 mm (sample C), and >1 mm (sample D). A portion of each sample was discarded by the sampling system onto the surface for examination. Discard pile A contained a fraction of the first scoop of sample that passed through the rover sampling system's 150 μm sieve. Discard pile B contained the fraction of the first scoop of sample that did not pass through the 150 μm sieve. Discard pile C
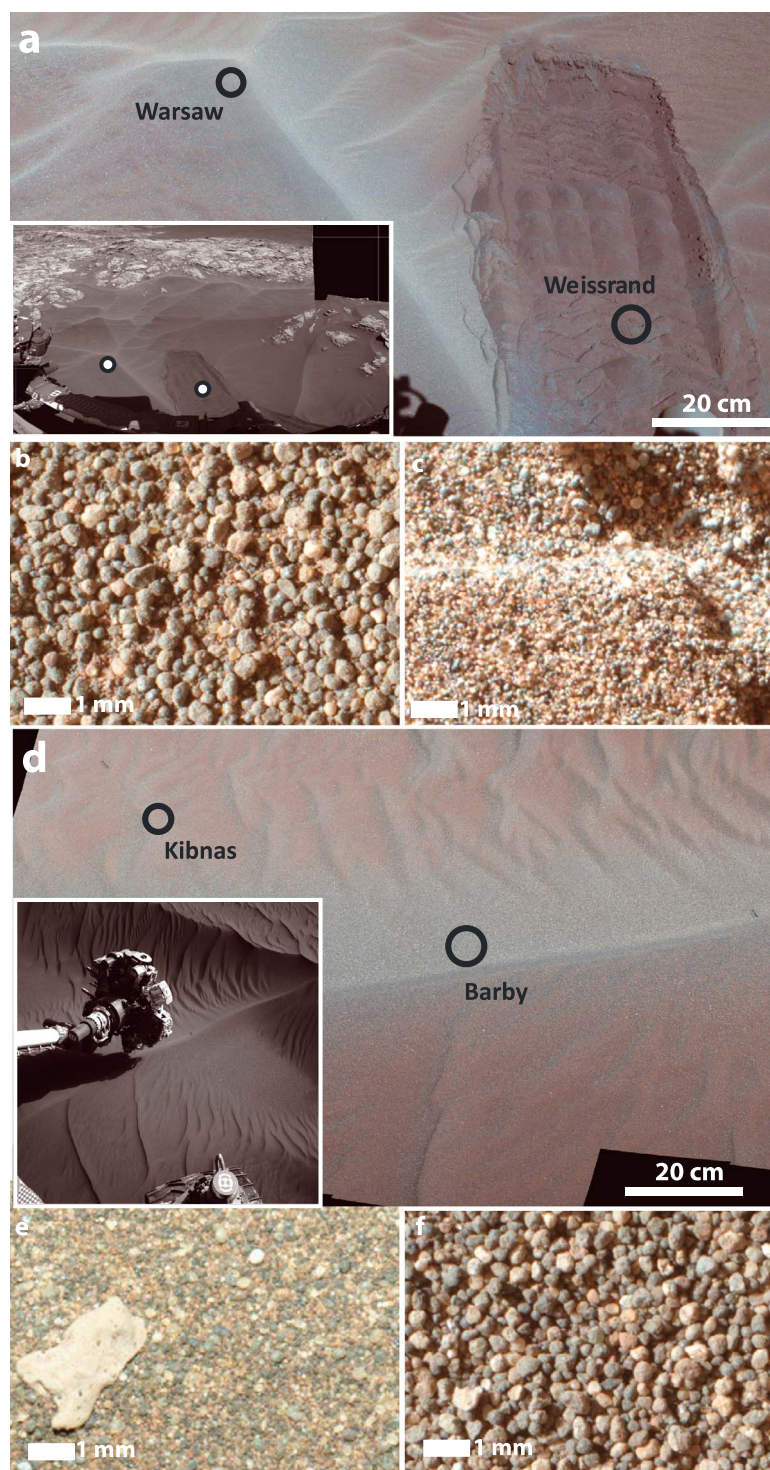
Figure 3. In situ measurements of aeolian sands were made at and near High dune. (a) A portion of a color Mastcam mosaic (from mcam05350; sol 1171) near High dune, showing targets Warsaw, the crest of a large ripple, and Weissrand, a rover wheel track through the sand (inset context image is a Navcam mosaic from sol 1181). Portions of MAHLI focus merge images of targets (b) Warsaw (natural illumination; 1182MH0005380000402862R00) and (c) Weissrand (natural illumination; 1182MH0005380000402830R00). (d) A portion of RGB color Mastcam mosaic (from mcam05372; sol 1184) on the stoss edge of High dune, showing targets Kibnas, a small ripple within a larger ripple trough, and Barby, the crest of a ripple (inset context image is a Navcam from sol 1184). Portions of MAHLI focus merge images of (e) Kibnas (night with white LED illumination; 1184MH0001630000402965R00) and (f) Barby (natural illumination; 1184MH0001630000402969R00). MAHLI products used are the dark-subtracted, flat-fielded, DRXX level processed data at resolutions in Table 2.

Table 1. Key Grain Size and Compositional Measurements in the Bagnold Dune Campaign as Part of the Systematic Full Suite of Measurements at Namib Dune at the Gobabeb Location[a]

Composition and Grain Size-Related Measurements
DAN active over Namib dune and additional measurements in the vicinity
CheMin X-ray diffraction of a <150 μm sample
SAM evolved gas analysis of a <150 μm sample
SAM evolved gas analysis of a 150 μm to 1 mm sample
APXS + MAHLI of undisturbed sands
APXS + MAHLI of disturbed, in-scuff sands
APXS + MAHLI Discard Piles A and E <150 μm
APXS + MAHLI Discard Piles B and F >150 μm
APXS + MAHLI Discard Pile C 150 μm to 1 mm
APXS + MAHLI Discard Pile D >1 mm (nonexistent; see text)
ChemCam Undisturbed Sand
ChemCam Across Ripples, Coarse to Fine
ChemCam Scuff (disturbed sands)
ChemCam Discard Piles A and E <150 μm
ChemCam Discard Piles B and F >150 μm
ChemCam Discard Pile C 150 μm to 1 mm to Discard Pile D, >1 mm, transect
Mastcam Multispectral and ChemCam Passive Scuff (disturbed sands)
Mastcam Multispectral and ChemCam Passive Discard Piles
Mastcam Multispectral and ChemCam Passive Undisturbed sands

[a]In addition, many opportunistic ChemCam data were acquired in and around the dunes [*Cousin et al.*, 2017]. For further details of rover activities during the Bagnold dune campaign, see *Bridges and Ehlmann*, [2017].

contained a fraction of the second scoop of sample that could not pass through the 150 μm sieve but that did pass through the 1 mm sieve, containing therefore a fractional split from 150 μm 1 mm. Discard pile D was intended to contain the fraction from the second scooped sample too coarse to pass through the 1 mm sieve. Discard pile D turned out to be essentially nonexistent, however, due to few or no particles larger than 1 mm. Discard piles E and F were originally intended with a third scoop to repeat the process used to generate C and D, as the team had originally intended two <1 mm aliquots to be delivered to the Sample Analysis at Mars instrument (SAM) for analyses of the coarse size fraction. However, an actuator anomaly prevented completion of these activities. When actuator use was again permitted, the third scoop was processed to size fractions like piles A and B but deposited at a different site to form piles E and F. Finally, relevant to interpreting the resultant grain sizes, any portion taken from the upstream side of the processing chain is only incompletely sieved; i.e., the >150 μm fraction typically will still retain some smaller grains, though the <150 μm split will always contain grains with at least two axes <150 μm.

Remote compositional science measurements with Curiosity's Mastcam and ChemCam and in situ science measurements with the Mars Hand Lens Imager (MAHLI) and Alpha-Particle X-ray Spectrometer (APXS) were conducted on discard piles A–F as well as undisturbed and disturbed sand surfaces. X-ray diffraction measurements with the Chemistry and Mineralogy (CheMin) instrument and SAM evolved-gas analysis measurements were made of ingested, processed samples. In conjunction with the campaign to assess composition and grain size, morphological and thermophysical properties of the dunes were assessed [*Lapotre et al.*, 2016; *Edwards et al.*, 2017; *Ewing et al.*, 2017], and monitoring of wind speed and potential dune activity was also implemented [*Newman et al.*, 2017; *Bridges et al.*, 2017; *Sullivan et al.*, 2017].

2.2. DAN

The DAN (Dynamic Albedo of Neutrons) experiment acquired measurements of scattered neutrons using both passive (natural) and active sources throughout the MSL mission to determine the H and Cl content of near-surface materials [*Mitrofanov et al.*, 2012, 2014; *Tate et al.*, 2015; *Litvak et al.*, 2016]. DAN acquired a series of measurements in the vicinity of the dune field near the boundary of the sedimentary rock substrate and dune sands, as well as a dedicated measurement directly over the dune. Upon departure from Namib dune on sol 1243, the rover was oriented backward over the workspace. In this configuration, the ~3 m diameter DAN active field of view was entirely over the sand. The resulting measurement with the active neutron source and detectors over Namib provides the best estimate of neutron response from bulk sand. Methods similar to *Sanin et al.* [2015] were used to analyze the DAN active measurements and model hydrogen content, reported as water-equivalent hydrogen, i.e., a wt % H_2O. Weight percent Cl was also estimated to an accuracy of 5–10 wt % (relative) [*Mitrofanov et al.*, 2014; *Litvak et al.*, 2016]. Because the depth of the DAN field of view extends ~60 cm into the subsurface, future investigation will involve detailed analysis of the depth of dune material below the rover during these active experiments, as well as the effect of the density contrast between the dune sands and the bedrock.

2.3. Mastcam

The focusable, fixed focal length (34 and 100 mm) Mastcam stereo multispectral imagers routinely provide visible-wavelength color data for drive planning, target selection, and studies of geomorphology, sedimentology, and stratigraphy [*Bell et al.*, 2012; *Malin et al.*, 2017]. Mastcam can also acquire 12-filter multispectral images over a visible/near-infrared (VNIR) wavelength range (400–1100 nm), enabling the detection and characterization of variations in iron-bearing mineralogy within Gale crater materials [e.g., *Wellington et al.*, 2017]. During the dune campaign, Mastcam multispectral data were acquired to characterize variation in the sand spectral properties and to measure and compare photometric properties of dune sands with other materials in Gale crater [*Johnson et al.*, 2017].

2.4. ChemCam

The ChemCam instrument collects passive visible/near-infrared (VNIR 400–840 nm) spectra and active laser-induced breakdown spectra (LIBS) with corresponding remote microscopic images [*Wiens et al.*, 2012; *Maurice et al.*, 2012; *Johnson et al.*, 2015]. The VNIR data provide similar information to Mastcam multispectral observations but with higher spectral resolution, while element emission lines in LIBS data from 240 to 850 nm provide chemical information over a 300–550 μm spot size. ChemCam was used to study the chemistry of the dunes in comparison to other fine materials measured at Gale crater [*Maurice et al.*, 2016]. LIBS data of major and select minor and trace elements were acquired of multiple sand targets [*Cousin et al.*, 2017]. ChemCam passive VNIR spectra were acquired and analyzed of the same targets [*Johnson et al.*, 2017].

2.5. MAHLI

The Mars Hand Lens Imager (MAHLI) is a focusable camera with a macro lens, deployed by the rover's robotic arm to acquire visible-wavelength color images at resolutions down to 14 μm/pixel of samples illuminated by natural light or UV or white light-emitting diodes (LEDs) [*Edgett et al.*, 2012]. The MAHLI focus merge products used in our figures were created onboard the instrument from eight-image focal plane stacks per the method described by *Edgett et al.* [2012]. MAHLI was used to examine the grain sizes of dune sands and characteristics such as roundness and to assess colors of grains to provide at least rudimentary information on their compositional diversity. MAHLI uses a Bayer pattern microfiltered RGB CCD (red, green, and blue charge coupled device), and color is interpolated between each broadband color-filtered pixel. The color of features within any given MAHLI image acquired with its dust cover open approximates true color under any illumination conditions, but, as with any camera, illumination conditions influence apparent color. On Mars, the scattered component of illumination is colored orangish-brown [*Thomas et al.*, 1999]. This affects the color of targets under all illumination conditions but is especially apparent for targets in shadow, where scattered light dominates. The truest color images are acquired when MAHLI white light LEDs illuminate a target at night, though these are still slightly blue relative to the response of the human eye to materials illuminated by sunlight [*Edgett et al.*, 2015]. The scales of features, including grain sizes, observed in MAHLI images and focus merge products are determined from focus position per the methods and equations described by *Edgett et al.* [2015].

2.6. APXS

The Alpha-Particle X-ray Spectrometer (APXS) is deployed by the rover arm on or just above a Mars surface target to acquire bulk elemental chemistry of targets [*Campbell et al.*, 2012; *Gellert and Clark*, 2015]. Similar instruments flew on the Mars Exploration Rovers (MERs) and observed materials at their landing sites [*Gellert et al.*, 2006]. Data for all major rock-forming elements and some minor and trace elements were acquired over a 1.7–3 cm spot size for the Bagnold dune targets and other Gale crater rocks and soils. Undisturbed, disturbed, and processed Bagnold sands were examined in detail as part of the campaign [*O'Connell-Cooper et al.*, 2017].

2.7. CheMin

The CheMin X-ray diffraction instrument [*Blake et al.*, 2012] examines the mineralogy of particulate samples, sieved to <150 μm and delivered to the instrument by the rover sample processing system. CheMin data are used to determine the type and abundance of crystalline phases, the elemental composition of major crystalline phases derived from refined unit cell parameters, and the relative proportions of amorphous and crystalline materials. CheMin previously measured the mineralogy of <150 μm Martian sands at the Rocknest

Table 2. Sand Grain Size Ranges Observed in Select MAHLI Images That Were Acquired of Sand Targets Near High Dune and on Namib Dune

Target (sol#_name)	Image Scale (μm/Pixel)	Type	Typical Grain Size Range (Diameter of Long Axis; μm)[a]	Additional Notes
High Dune Samples				
1182_Warsaw	18.9	undisturbed, ripple	150[b]–900	
1182_Weissrand	21	track	40[c]–200	
1184_Barby	22.5	undisturbed, ripple	150–600	Also, two 800–900 μm size grains
1184_Kibnas	25.9	undisturbed, trough	50[c]–400	One 3 mm clast, a light-toned rock fragment
Namib Dune Samples				
1226_GB cand. Scoop site #2	20.7	APXS touch	40–500	one ~1 mm grain that looks like a broken off rock clast
1242_Otavi	16	undisturbed, ripple	60–450	
1228_GB wheel scuff	16.7	scuff	80–350	
1241_GB_discardA	15.7	processed to <150 μm	45–250	
1230_GB_discardB	17.4	processed to >150 μm	80–420	some finer grains on lower left, off of discard pile
1242_GB_discardC	16	processed to 150 μm to 1 mm	50–600	
1242_GB_discardD	16.4	processed to >1 mm	80–500	rare <60 μm grains
1253_GB_discardE	21.4	processed to <150 μm	40–200	two ~300 μm spherical grains
1253_GB_discardF	22.1	processed to >150 μm	100–500	one ~1 mm grain

[a]Each MAHLI image product has an associated μm/pixel scale in the header, calculated from the distance to target and focus. Size was measured for the ~15 largest and ~15 smallest grains in the images to obtain the minimum and maximum. Because most grains are quasi-spherical, the long axis is typically similar the average axis.
[b]Some grains in between larger grains may be below the limit of resolution.
[c]Some grains are below the limit of resolution.

bedform [*Blake et al.*, 2013; *Bish et al.*, 2013] and <150 μm powders drilled from sedimentary rocks in Gale crater. At Namib dune, CheMin measured the mineralogy of the <150 μm sieved sample (Gobabeb sample A, GB_A) [*Achilles et al.*, 2017].

2.8. SAM

The Sample Analysis at Mars instrument suite includes a quadrupole mass spectrometer, a tunable laser spectrometer, and a six-column gas chromatograph [*Mahaffy et al.*, 2012]. SAM has been used for multiple measurements along Curiosity's traverse, including determination of the chemistry and isotopic composition of rocks and sands [e.g., *Leshin et al.*, 2013; *Ming et al.*, 2014; *Sutter et al.*, 2017]. SAM evolved gas analyses (EGAs) were acquired of the <150 μm sample (GB1, from the same portion as Gobabeb sample A) and the 150 μm–1 mm sample (GB2, from a similar portion to Gobabeb sample C) [*Sutter et al.*, 2017]. The GB1 sample was three aliquots, nominally 75 mm^3 each, of <150 μm sample. The GB2 sample was expected to be two aliquots, nominally 130 mm^3 each, of <150 μm to 1 mm sample, but an actuation fault meant that only the first aliquot was included in the delivery. Because of the atypical delivery scenario for the coarse fraction, where the actual amount of material reaching the sample cup is ill-constrained, we show EGA curves but do not present quantitative weight percent for volatiles in GB2. The GB1 sample size is—as with all delivered samples—of somewhat uncertain volume. The triple aliquot portion was assumed to be 135 ± 31 mm^3, based on results from testbed deliveries, for weight percent computations of volatiles in GB1 [*Sutter et al.*, 2017]. Both GB1 and GB2 samples were subjected to ramped heating to a final temperature of about 870°C while the quadrupole mass spectrometer was continuously scanned. This allows the identification and quantification of gases released from the sample upon heating.

3. Results

3.1. Grain-Scale Properties: Sizes and Colors

MAHLI measurements of natural and robotically disturbed surfaces show that grain size sorting by wind has occurred in the Bagnold dune field (Table 2). Additional size distribution data are included for a subset of these samples in *Edwards et al.* [2017] and *Cousin et al.* [2017]. Near High dune, ripples are composed mostly of fine to medium sand (125–500 μm) that is darker and grayer than surrounding sands, as shown in the MAHLI images of targets named Warsaw and Barby (Figures 3a, 3b, 3d, and 3f). A few smaller grains located between larger grains at the Warsaw site are below the resolution of acquired images; i.e., grains are smaller

than 60–80 μm. A ripple trough target, Kibnas, contains many finer, unresolved grains, along with rare scattered pebbles that apparently are rock fragments (e.g., Figure 3e). At Weissrand, within tracks where sands were disturbed by the rover wheel, all grains are fine sand and smaller (<200 μm; Figure 3c).

Grains are more well-sorted at Namib dune near the Gobabeb (GB) sampling site (Figure 2b). For two undisturbed sand targets (GB scoop site and Otavi) and one disturbed sand target (GB wheel scuff), the grain size ranges from coarse silt (~45 μm) to medium sands (~500 μm) (Table 2 and Figure 4). Upon scooping and processing of Gobabeb samples into grain size separates, ample quantities of sample were produced for all but the >1 mm fraction (sample D). This observation is consistent with MAHLI images showing that >1 mm grains are typically absent at the Gobabeb site. Analyses of all targets at Gobabeb indicate that the maximum grain size is typically 400–600 μm. Grains smaller than 45–60 μm in size are absent in undisturbed, disturbed, and sieved fractions (Table 2 and Figure 4). The highest-resolution MAHLI images of a geologic target on Mars acquired to date (15.6 μm/pixel) were obtained from discard pile A (GB_A; sieved to <150 μm) at a 5 mm standoff (Figures 5 and 6). Although lacking its coarsest fraction because of sieving, GB_A is otherwise similar in appearance to the disturbed samples. Manual counts show that grain long axes range from ≥45 μm to ≤220 μm with a mode near 120 μm (Figure 5 and Table 2). Grains finer than the resolution limit of ~45 μm are not present. The size distribution of the Namib dune sands contrasts with that of Rocknest and prior in situ investigations of Martian fines, where silt-sized particles and smaller were major components of soils (see section 4.1). Grain sizes for the undisturbed sand surface imaged at Otavi and disturbed sands in the Gobabeb wheel scuff are similar (Figure 4 and Table 2). This indicates that grain sizes of the Namib dune surface and its bulk interior are similar, although Mastcam images suggest that coarser grains are present at larger ripple crests (Figure 6).

Grains are rounded to subrounded at all grain sizes and for all samples (Figure 4). In MAHLI images of sands at the Bagnold dune study site, we observe multiple colors of grains: opaque gray of various shades, translucent yellow, opaque reddish, opaque white or light gray, translucent green, and translucent colorless (Figure 4). Opaque gray grains are the most abundant, comprising approximately half of the samples, determined by qualitative visual inspection of all MAHLI data as well as counts on the sample A discard pile at Gobabeb (Figure 5). Yellow translucent and reddish opaque grains are next most abundant, and opaque white grains comprise <10% of the sample. Translucent green and translucent clear grains are rare. The size distribution of the opaque reddish grains is slightly smaller than the other colors, and they comprise less of the sample in the coarser sieved fractions (B, C, and D; Figures 4d–4f) and more on undisturbed surfaces (e.g., Figures 4a and 4b). Nevertheless, all grain colors are observed in all samples.

3.2. Spectral Properties

Visible and near-infrared wavelength albedo variations in dune materials imply differences in composition or grain size between undisturbed samples, disturbed samples, and Gobabeb samples A, B, C, and D. Variations in multispectral reflectance and ChemCam VNIR spectra of sands correlate with variations in visible color and grain size noted previously; i.e., the coarser fractions are grayer (Figure 6). The sand spectra have a reflectance of <0.1 and rise in reflectance from 400–500 nm (blue/green) to 600–700 nm (red), before decreasing in VNIR reflectance toward 1000 nm (Figure 6b). The same spectral shape is seen in Mastcam data, ChemCam passive VNIR data [see *Johnson et al.*, 2017], and Compact Reconnaissance Imaging Spectrometer (CRISM) data acquired from orbit [*Lapotre et al.*, 2017]. The Gobabeb sample A discard pile (<150 μm) has a similar spectral shape as typical Martian fine-grained materials but is less red and with a more pronounced absorption near 1000 nm. Coarser-grained samples B, C, and D exhibit even lower reflectance at infrared wavelengths, a slightly higher reflectance in the visible blue-green wavelengths, a flattening in the spectra from 600 to 700 nm, and a broader 1000 nm absorption, beginning at a shorter wavelength than in sample A. As described further in *Johnson et al.* [2017], the observed differences in spectral properties are consistent with greater relative proportions of olivine, and potentially other mafics, in the coarser discard piles, a trend also seen in chemical data (section 3.4). Another factor contributing to dune spectral properties is the presence or absence of aeolian dust. The Namib dune sands (Figure 4) are typically darker than the High dune sands and nearby sand patches (Figure 3), which have orangish-brown dust on surfaces. Although not readily apparent in visible color MAHLI and Mastcam images of Namib dune (Figure 2b), undisturbed and disturbed sands have slightly different infrared color properties (Figure 6a), perhaps indicating a small amount of dust present on the Namib surface as well.
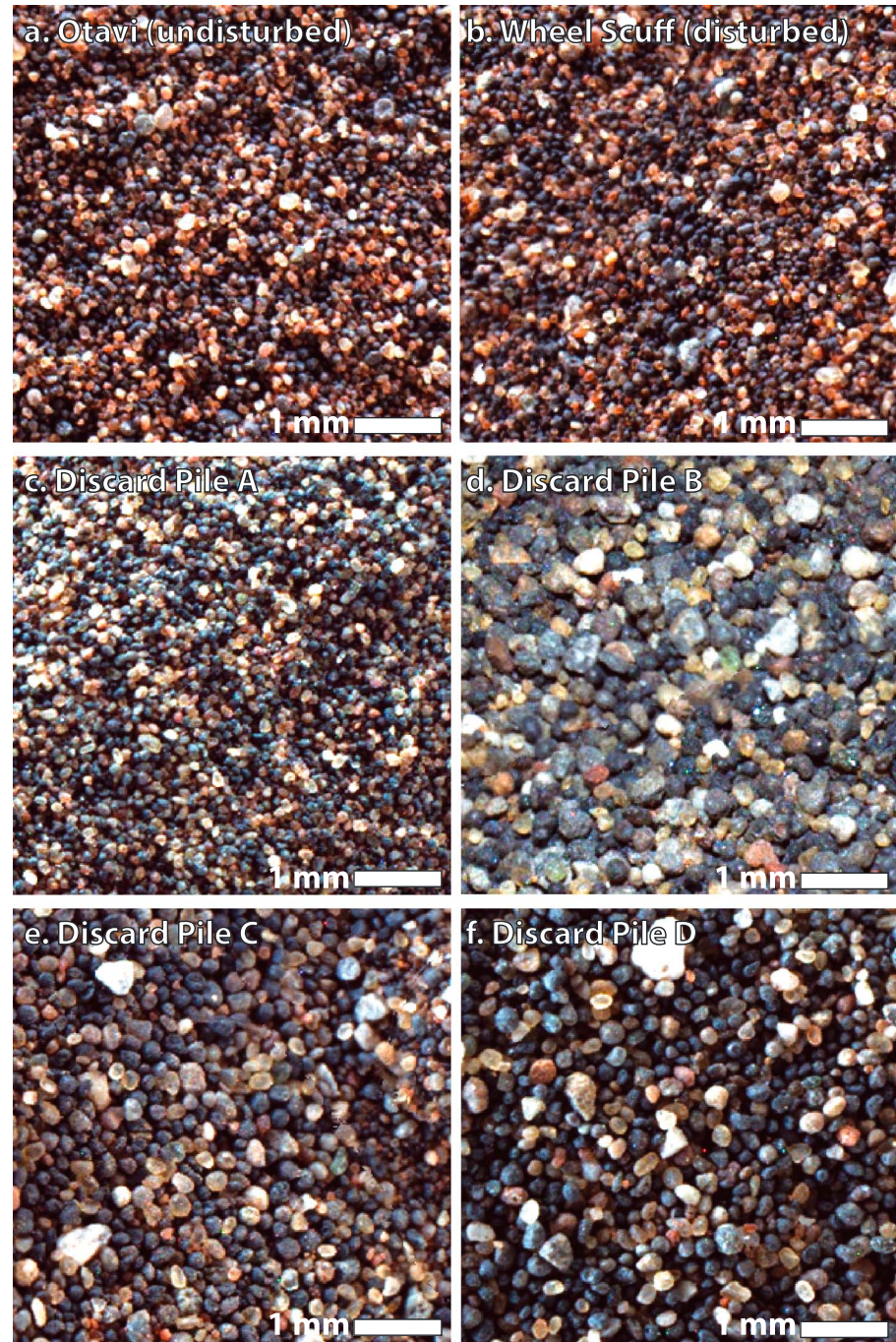
Figure 4. MAHLI focus merge products of sands at the Gobabeb investigation site on the lower north side of Namib dune, each with a linear 2% stretch applied on the whole image. (a) Undisturbed sands at the Otavi target (1242MH0005740000403707R00), (b) disturbed sands within a wheel scuff (1228MH0001700000403450R00), (c) sieved sands of sample discard pile A (<150 µm sieved fraction from Scoop 1; 1242MH0005740000403723R00), (d) sieved sands of discard pile B (>150 µm fraction from Scoop 1; 1231MH0001630000403553R00), (e) sieved sands of discard pile C (150 µm-1 mm sieved fraction from Scoop 2; 1242MH0005740000403711R00), and (f) over the expected location of the discard pile D (processed to >1 mm from Scoop 2; 1242MH0005740000403709R00). Most images were acquired from ~1 cm standoff distance with the exception of Figure 4c (discard pile A), which was acquired from ~5 mm standoff distance. The pixel scales are similar between images (15.6–17.5 µm/pixel). Opaque gray, translucent yellow, opaque red, and opaque white grains are most typically observed with rarer translucent green and translucent white grains. Products used are the dark-subtracted, flat-fielded, DRXX level processed data at resolutions in Table 2.
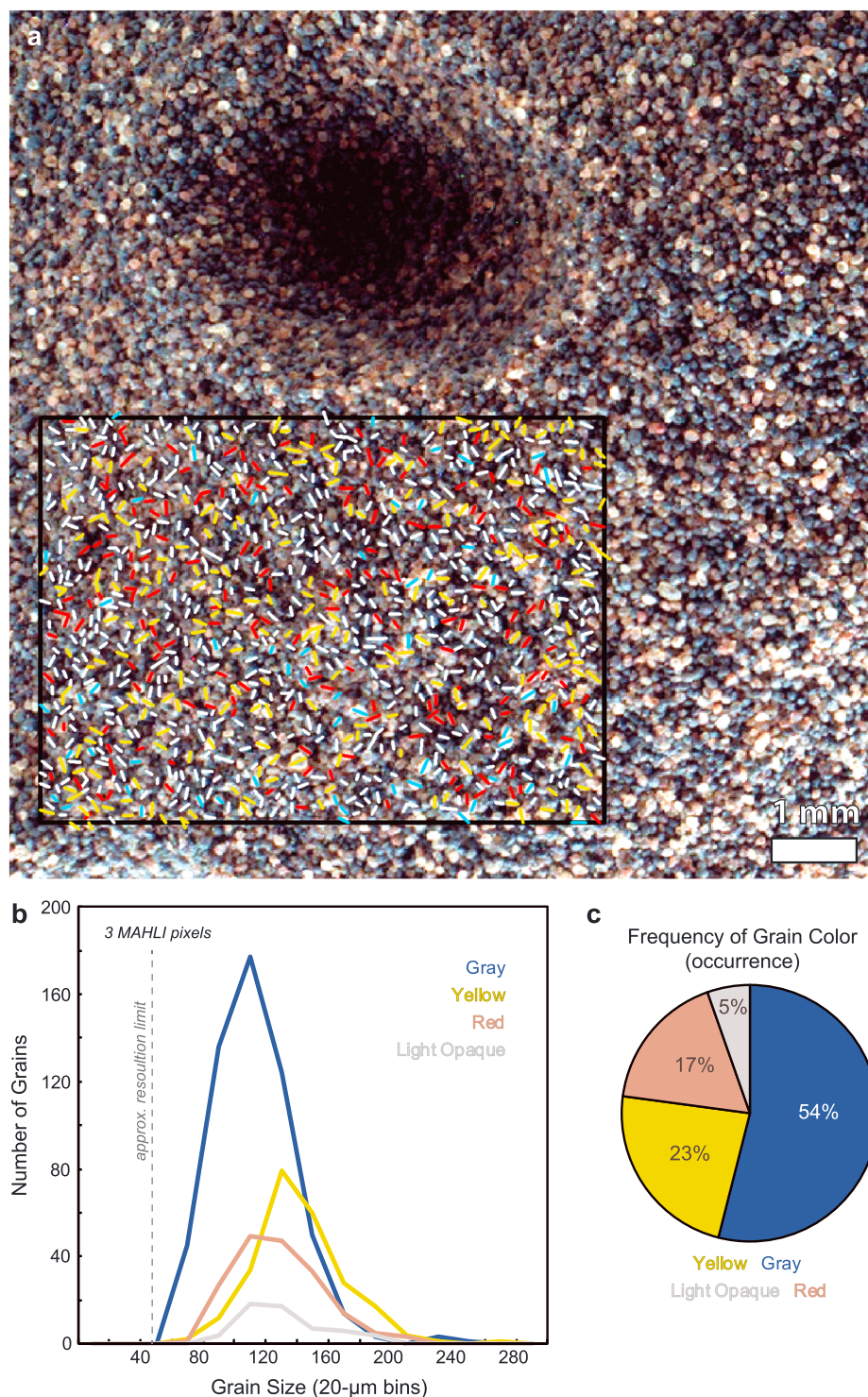
Figure 5. (a) A portion of a MAHLI focus merge product showing sieved sands from Gobabeb scoop sample 1, discard pile A (1242MH0005740000403723R00; 15.7 μm/pixel), showing the ~30 mm² area over which we made grain color occurrence estimates. The depression (top, left of center) is from a series of ChemCam LIBS shots into the discard pile, leaving behind a pit from laser interaction and plasma production. (b) The number of grains and size distribution by color of all 1023 grains catalogued; the distribution is well above the MAHLI threshold resolution for resolving grains. (c) A summary of the relative frequency of each color grain.
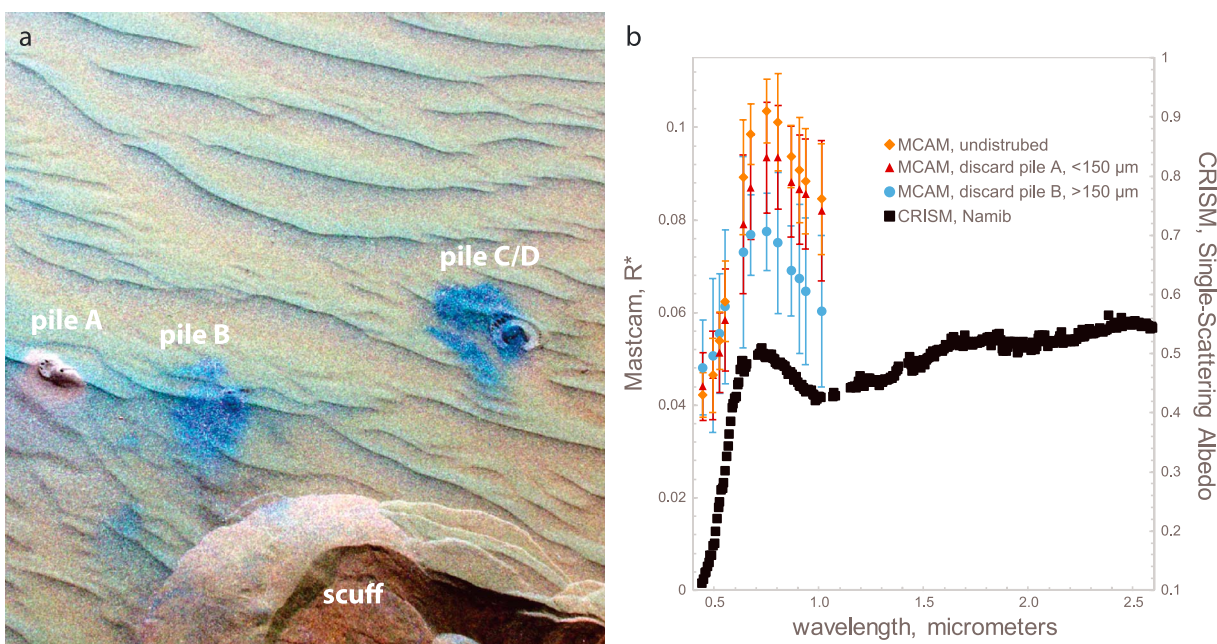
Figure 6. (a) Mastcam false color image (from mcam5707 on sol 1234 with narrowband filters L6: 1012 nm; L4 676 nm; and L2: 445 nm as red, green, and blue, respectively) of sands at Gobabeb, Namib dune, which shows subtle visible/near-infrared color differences in a portion of the scuff and the discard piles for samples A (<150 μm), B (>150 μm), C (150 μm to 1 mm), and D (>1 mm) (see text). (b) Mastcam spectra from locations corresponding to Figure 6a in units of R-star, a proxy for reflectance [*Johnson et al.*, 2017], along with processed CRISM single-scattering albedo spectra from the Namib dune from CRISM image ATO0002EC79 [*Lapotre et al.*, 2017]. The spectral shape is similar to CRISM data.

3.3. Bulk Mineralogy (<150 μm Fraction)

The mineralogy of the size fraction equivalent to Gobabeb discard pile A (<150 μm), measured by CheMin, is typical of a basalt. The dominant crystalline phases are Na,Ca-feldspar (~37 wt %), olivine (26 wt %), and two pyroxenes (22 wt % augite and 11 wt % pigeonite). Minor phases, each present at ≤2%, include anhydrite, magnetite, hematite, and quartz. These data and further CheMin mineralogical analyses are detailed in *Achilles et al.* [2017]. The bulk mineralogy of the Gobabeb sample is, overall, quite similar to sands from Rocknest (Figure 7). Minor differences at approximately the level of analytical uncertainty include a greater
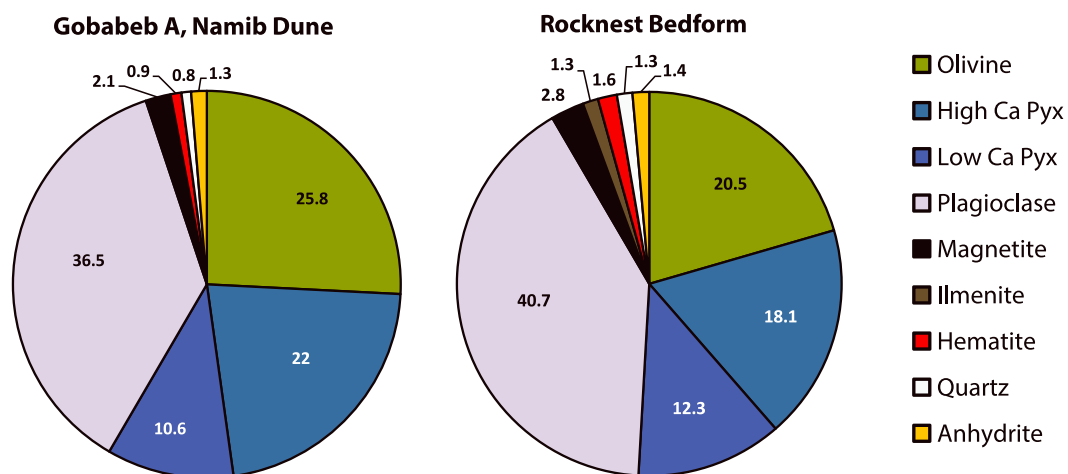

Figure 7. The mineralogy (wt %) of crystalline phases measured by CheMin, comparing Rocknest and Namib dunes (sample Gobabeb A). The estimated amorphous material content of both Gobabeb and Rocknest is 35% ± 15%. Data from Gobabeb are from *Achilles et al.* [2017]; data from Rocknest are from *Achilles et al.* [2017] as updated from *Bish et al.* [2013], using a new CheMin calibration.
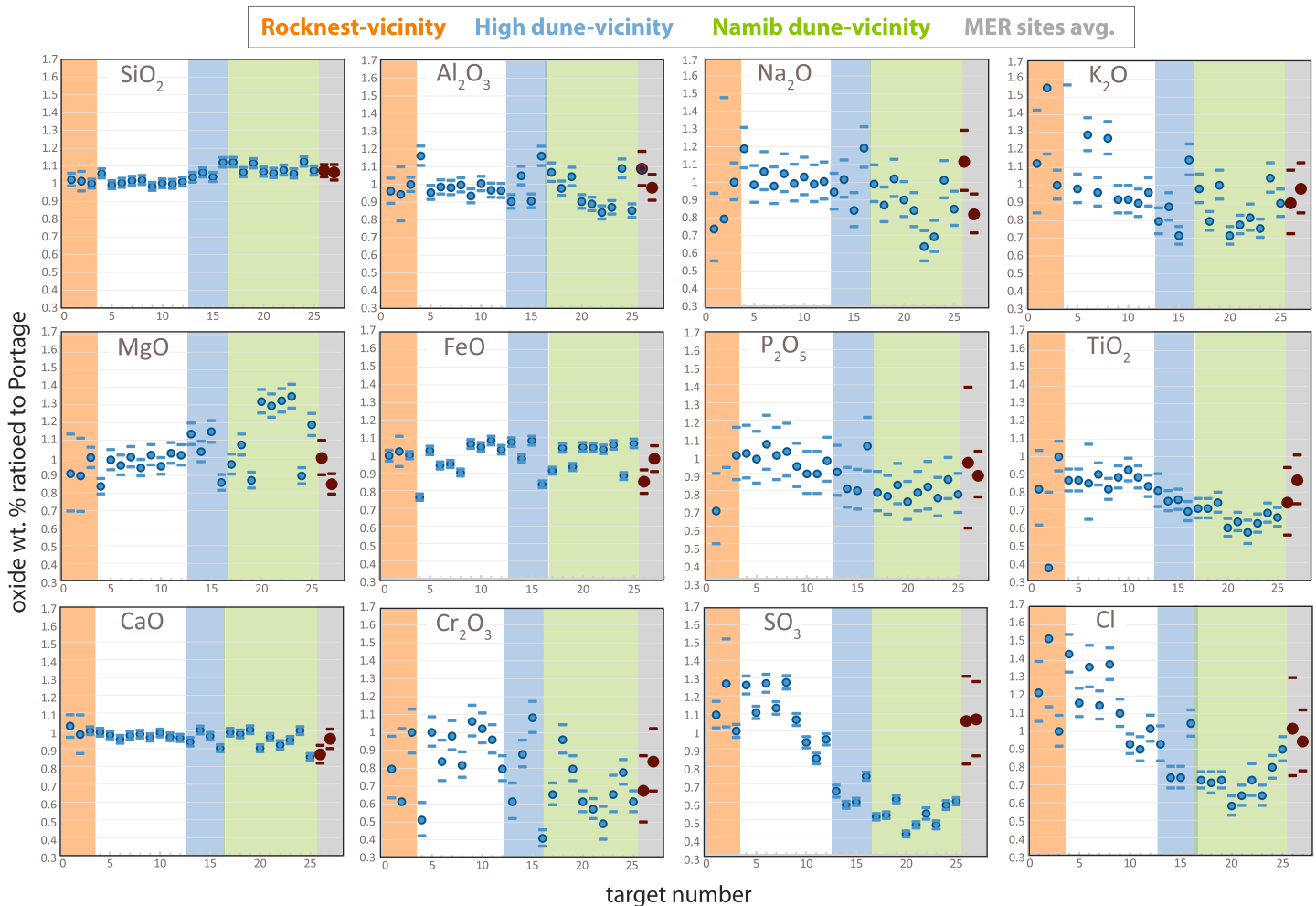
Figure 8. Bulk APXS chemistry for select elements of all Gale unconsolidated targets, as well as average soils from the Mars Exploration Rover Spirit and Opportunity sites [*Morris et al.*, 2006a, 2006b] normalized to Portage at Rocknest. Soils in the vicinity of Rocknest, High Dune, and Namib dune are indicated by colors. For Rocknest, the order of targets is unscuffed, scuffed, and Portage; note that high temperatures and large standoff distances degrade the quality of the first two samples. For High dune, the order of targets displayed is Warsaw, Weissrand, Kibnas, and Barby. For Namib dune, the order of targets displayed is scuff, scoop2, and discard piles A, D, C, B, C2, E, and F. Target details by number are in Table 3.

ratio of low- to high-calcium pyroxenes in Rocknest, an ~5 wt % greater plagioclase content in Rocknest, an ~5 wt % greater olivine content in Gobabeb, and ilmenite at ~1 wt % in Rocknest not present in the Gobabeb sample. Both the Gobabeb and Rocknest samples also have a large amorphous component (noncrystalline or poorly crystalline) of 35 ± 15 wt %.

3.4. Chemical Composition of the Dune Sands
3.4.1. Major and Minor Elements

Namib dune is composed of olivine basaltic sand, as anticipated by analysis of observations acquired by orbiter-borne spectrometers [*Rogers and Bandfield*, 2009; *Anderson and Bell*, 2010; *Milliken et al.*, 2010; *Lane and Christensen*, 2013; *Seelos et al.*, 2014; *Lapotre et al.*, 2017]. The composition is broadly similar to that of other Martian aeolian sands and soils; however, detailed comparisons of the chemistry of Namib dune samples with other fine-grained soils analyzed at Gale crater and by the MER rovers at their landing sites show that most of the Bagnold dune sands are compositionally distinct. ChemCam data show that the dune sands have, on average, higher Fe and Mn than prior soils examined at Gale crater [*Cousin et al.*, 2017]. Namib dune sands also have higher weight percent oxide totals, likely pointing to a lack of volatile elements relative to previously measured soils [*Cousin et al.*, 2017]. APXS bulk data show that Namib dune aeolian sands are enriched in Si, Mg, and Ni and depleted in Al, Na, K, Cr, Ti, Zn, S, and Cl relative to other

Gale soils (Figure 8 and Table 3). Note that the four High dune targets measured by APXS do not share the same characteristics as the Namib dune sand targets in that they are not enriched in Mg, and a few of the targets are enriched in Na, K, and Al relative to most other soils at Gale crater (Figure 9). Bulk chemistry is further described in *O'Connell-Cooper et al.* [2017] and *Cousin et al.* [2017].

3.4.2. Volatile Content

The depletion of sulfur and chlorine in Bagnold dune sands, especially at Namib dune, is significant. Many APXS-measured chlorine values and all sulfur values are lower than even 1σ bounds on soils measured by MER rovers at Gusev crater and Meridiani Planum [*Morris et al.*, 2006a, 2006b]. A principal component analysis (PCA) of APXS analyses of the sands illustrates that enrichment in Si and depletion in S and Cl are the most important chemical differentiators between Namib dune sands and other Mars sands and soils, including the fine-grained materials analyzed at the Rocknest (target named Portage) (Figure 9). The Bagnold dunes are low in these elements, consistent with higher ChemCam total oxide weight percentages [*Cousin et al.*, 2017].

Collectively, the compositional data indicate depletion of many volatiles in bulk analyses of Namib dune targets relative to other Gale samples. DAN neutron data show that the hydrogen content at the dunes is the lowest measured on the mission through sol 1600 (0.8 wt % water equivalent, uniformly distributed in the upper 60 cm; Figure 10a), and the chlorine content is similarly low (~0.5 wt %; Figure 10b) [*Mitrofanov et al.*, 2014; *Litvak et al.*, 2016]. ChemCam also observed lower hydrogen peaks in the dune material than in previous soils [*Cousin et al.*, 2017]. Similarly, evolved gas analyses from SAM indicate that water is present at 1.1 ± 0.3 wt % (Figure 11). This is ~1 wt % lower than in the Rocknest sample and among the lowest at Gale crater measured to date [*Sutter et al.*, 2017] (Figure 11b). Analysis of evolved gases as a function of temperature show little water release at temperatures below 200°C for Gobabeb. This contrasts with the Rocknest sample and many phyllosilicate- and silica-bearing samples from rocks, where lower temperature water release is substantial (Figure 11a) [*Leshin et al.*, 2013; *Sutter et al.*, 2017]. Both the coarse and the fine samples from the Namib dunes have similar profiles with a peak evolved H_2O at approximately 400°C and some H_2O released over the whole range from 150 to 800°C (Figure 11).

Evolved SO_2 from the fine fraction (reported as 1.2 ± 0.3 wt % SO_3) was about 50% less than Rocknest and less also than most Gale crater rocks [*Sutter et al.*, 2017]. Sulfur dioxide evolved between 550 and 825°C which is consistent with the presence of Fe sulfates and Mg sulfates or Al sulfates (Figure 12). Although CheMin analysis shows the presence of anhydrite [*Achilles et al.*, 2017], crystalline Ca sulfate pyrolysis temperatures are too high for the SAM instrument and would not contribute to the totals. Interestingly, the coarse-grained Gobabeb sample has a lower SO_2 release temperature than the fine-grained sample, possibly indicating a difference in the dominant cation associated with the sulfates. Additionally, the coarse dune sample shows a lower temperature peak at 350–550°C, consistent with the oxidation of sulfides [*Sutter et al.*, 2017] (Figure 12).

Evolved CO is also less than Rocknest, by several factors, and is among the lowest measured so far on the mission (Figure 13), possibly indicating lower trace organics content [*Sutter et al.*, 2017]. Not all volatiles are depleted in the Gobabeb sample, however. Similar quantities of evolved CO_2 and NO are observed for the Rocknest and Gobabeb samples, which are higher than for most of the sedimentary rocks analyzed by SAM (Figure 13) [*Sutter et al.*, 2017]. However, differences in the constituent materials responsible for CO_2, CO, and NO are indicated by different release temperature profiles in Gobabeb versus Rocknest (Figure 13). For example, at Gobabeb there is little CO_2 and CO released at temperatures <400°C, compared to Rocknest and most Gale sedimentary rocks [*Sutter et al.*, 2017]. This indicates that the release of CO_2 in Gobabeb is consistent with carbonate mineral decomposition, which is known to occur at $T > $ ~400°C, though a contribution from organics cannot be ruled out [*Sutter et al.*, 2017].

3.4.3. Grain-Scale and Grain Size-Dependent Chemical Variation

Major and minor element data also indicate that the chemical compositions of Namib sands vary with grain size (Figure 14a). In data normalized to GB_A (smallest mean grain size), APXS bulk data show that the Namib dune sands with larger mean grain sizes are notably enriched in Mg and Ni. The coarse fraction is also enriched in Fe and Mn, according to ChemCam [*Cousin et al.*, 2017], an effect seen subtly in APXS data (Figure 14a). Br is enriched, while Al, Ti, Ca, Na, K, Cr, and Zn are depleted in APXS chemistry of Gobabeb's coarsest size factions. The patterns of element enrichment and depletion as a function of mean grain size differ from that expected solely by admixture of dust, based on prior analyses using MER data [*Yen et al.*, 2005].

Table 3. APXS Target Data Used in Figures 8 and 9 With MER Soil Values From *Morris et al.* [2006a, 2006b]

| Sol	Target	Na_2O	Error	MgO	Error	Al_2O_3	Error	SiO_2	Error	P_2O_5	Error	SO_3	Error	Cl	Error	K_2O	Error
58	(Rocknest) Scuffed_E	1.99	0.41	7.9	1.67	9.02	0.48	43.94	0.96	0.65	0.14	5.97	0.3	0.84	0.08	0.55	0.12
58	(Rocknest) Unscuffed_A	2.14	1.64	7.79	1.58	8.84	1.25	43.54	1.82	0	0.82	6.93	1.23	1.05	0.23	0.76	0.16
89	(Rocknest) PortageRP	2.7	0.14	8.69	0.25	9.37	0.19	42.97	0.54	0.95	0.07	5.47	0.1	0.69	0.03	0.49	0.02
373	Maya	3.21	0.14	7.27	0.17	10.88	0.29	45.41	0.54	0.96	0.07	6.89	0.15	0.99	0.03	0.84	0.04
523	King_rp	2.66	0.14	8.58	0.25	8.94	0.19	42.68	0.43	0.93	0.07	6.04	0.08	0.8	0.02	0.48	0.02
530	Barker	2.86	0.14	8.31	0.25	9.23	0.19	43.15	0.54	1.01	0.07	6.94	0.15	0.94	0.04	0.63	0.02
531	Argyle	2.64	0.14	8.72	0.25	9.2	0.19	43.66	0.54	0.95	0.07	6.18	0.08	0.79	0.02	0.47	0.02
558	Johnny_Cake_rp	2.83	0.14	8.18	0.17	9.34	0.19	43.83	0.54	0.97	0.07	6.97	0.08	0.95	0.02	0.62	0.02
605	Lagrange	2.68	0.14	8.82	0.25	8.76	0.19	42.29	0.43	0.89	0.05	5.82	0.08	0.76	0.02	0.45	0.02
673	Sourdough_RP	2.78	0.14	8.27	0.17	9.41	0.19	43.05	0.54	0.85	0.05	5.12	0.08	0.64	0.01	0.45	0.02
801	Kelso	2.67	0.14	8.91	0.25	9.06	0.19	42.89	0.54	0.85	0.05	4.62	0.08	0.62	0.02	0.44	0.02
802	Dumont	2.71	0.14	8.81	0.25	9.04	0.19	43.43	0.54	0.92	0.05	5.21	0.08	0.7	0.02	0.47	0.02
1182	Warsaw	2.55	0.14	9.85	0.25	8.46	0.19	44.48	0.64	0.86	0.07	3.61	0.12	0.64	0.04	0.39	0.02
1182	Weissrand	2.74	0.14	8.98	0.25	9.83	0.29	45.69	0.54	0.77	0.05	3.19	0.05	0.51	0.02	0.43	0.02
1184	Kibnas_APXS	2.27	0.14	9.97	0.25	8.49	0.19	44.56	0.54	0.76	0.05	3.28	0.05	0.51	0.02	0.35	0.01
1184	Barby_RP	3.22	0.14	7.46	0.17	10.87	0.29	48.11	0.54	1	0.07	4.07	0.05	0.72	0.02	0.56	0.02
1223	Gobabeb_Scuff_APXS	2.67	0.14	8.36	0.25	10.01	0.29	48.15	0.54	0.75	0.05	2.82	0.05	0.5	0.01	0.48	0.02
1225	Gobabeb_Scoop2_RP	2.35	0.14	9.32	0.25	9.16	0.19	45.74	0.54	0.73	0.05	2.87	0.05	0.49	0.02	0.39	0.01
1226	Gobabeb_DumpA_APXS	2.75	0.14	7.57	0.17	9.78	0.29	47.88	0.54	0.79	0.05	3.36	0.05	0.5	0.01	0.49	0.02
1230	Gobabeb_DumpD	2.43	0.14	11.46	0.25	8.46	0.19	45.85	0.54	0.7	0.05	2.29	0.05	0.4	0.02	0.35	0.01
1241	Gobabeb_DumpC	2.27	0.14	11.24	0.25	8.33	0.19	45.53	0.54	0.75	0.05	2.57	0.05	0.44	0.02	0.38	0.01
1242	Gobabeb_DumpB	1.72	0.14	11.5	0.25	7.88	0.19	46.24	0.64	0.78	0.07	2.92	0.12	0.5	0.04	0.4	0.02
1242	Gobabeb_DumpC_corrected	1.87	0.14	11.71	0.25	8.15	0.19	45.42	0.54	0.72	0.05	2.57	0.08	0.44	0.02	0.37	0.01
1253	Gobabeb_DumpE	2.73	0.14	7.79	0.17	10.21	0.29	48.31	0.54	0.82	0.05	3.18	0.08	0.55	0.02	0.51	0.02
1253	Gobabeb_DumpF	2.29	0.14	10.31	0.25	7.98	0.19	46.13	0.54	0.74	0.05	3.3	0.05	0.62	0.02	0.44	0.02
	Gusev	3.01	0.3	8.67	0.6	10.2	0.7	46.1	0.9	0.91	0.31	5.78	1.25	0.7	0.16	0.44	0.07
	Meridiani	2.21	0.18	7.38	0.29	9.2	0.5	45.7	1.3	0.84	0.06	5.83	1.04	0.65	0.09	0.48	0.05
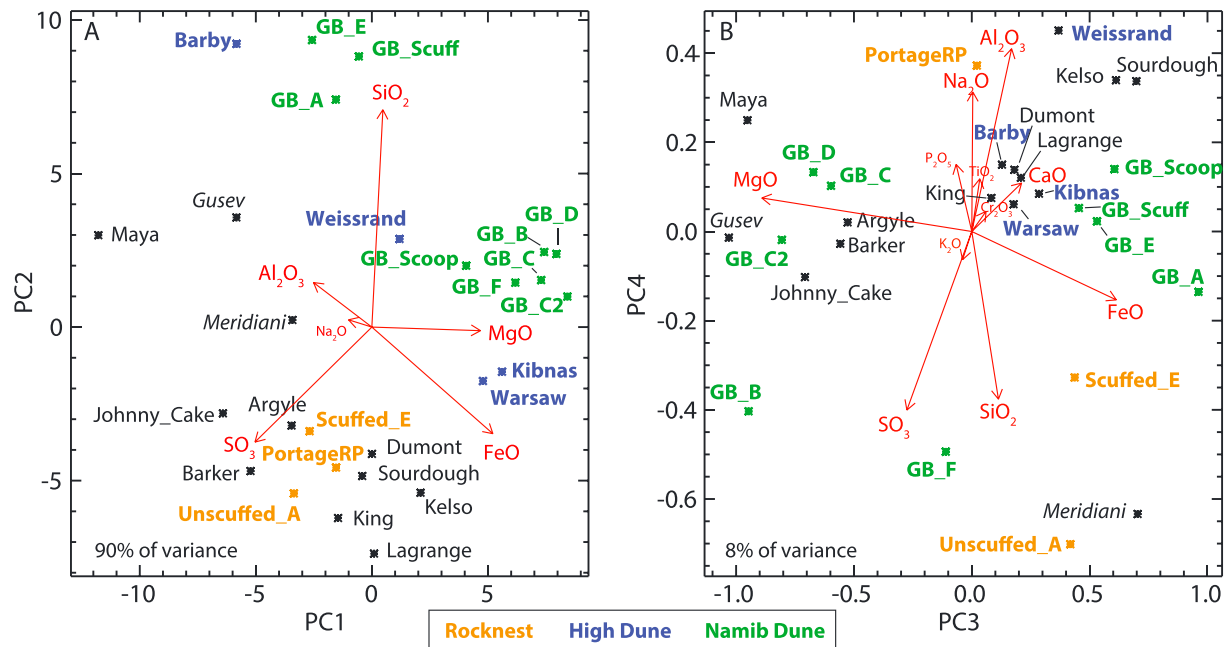
Figure 9. Principal component analysis biplots of APXS of Gale soil targets with oxides contributing to each factor highlighted for (a) principal components 1 and 2 and (b) principal components 3 and 4. Soils in the Rocknest area from Bradbury Rise and High and Namib Dunes are color coded. Gusev and Meridiani average soil compositions are also plotted for comparison. Data were normalized to the mean for each oxide prior to PCA computation. Line length for each factor (the oxide vector transformed into the eigenvector coordinate axes) is proportional to its importance in accounting for the data variance within each principal component. Chemical data included in this PCA were Na_2O, MgO, Al_2O_3, SiO_2, P_2O_5, SO_3, K_2O, CaO, TiO_2, Cr_2O_3, and FeO.

Table 3. (continued)

CaO	Error	TiO$_2$	Error	Cr$_2$O$_3$	Error	MnO	Error	FeO	Error	Ni	Error	Zn	Error	Br	Error
7.45	0.38	0.97	0.21	0.39	0.06	0.39	0.04	19.13	0.39	436	115	544	70	0	5
7.11	0.71	0.44	0.47	0.3	0.17	0.5	0.09	19.58	1.44	649	299	649	179	0	0
7.26	0.08	1.19	0.05	0.49	0.03	0.42	0.02	19.18	0.2	456	30	326	15	34	10
7.2	0.08	1.03	0.03	0.25	0.03	0.31	0.02	14.62	0.2	340	30	383	20	48	10
7.09	0.08	1.03	0.03	0.49	0.01	0.42	0.01	19.7	0.26	645	35	309	10	41	5
6.91	0.08	1.01	0.21	0.41	0.03	0.41	0.02	18.07	0.2	498	35	375	20	49	10
7.07	0.08	1.07	0.03	0.48	0.01	0.41	0.01	18.23	0.2	452	24	308	10	43	5
7.12	0.08	0.97	0.03	0.4	0.01	0.38	0.01	17.3	0.2	432	24	381	15	74	5
6.99	0.07	1.05	0.03	0.52	0.01	0.44	0.01	20.4	0.26	557	30	283	10	23	5
7.17	0.08	1.1	0.03	0.5	0.01	0.44	0.01	20.09	0.26	516	30	355	15	26	5
7.01	0.08	1.05	0.03	0.47	0.01	0.44	0.01	20.77	0.26	557	30	287	15	49	5
6.97	0.07	0.99	0.03	0.39	0.01	0.42	0.01	19.78	0.26	542	30	276	10	43	5
6.81	0.1	0.96	0.07	0.3	0.03	0.38	0.02	20.61	0.26	821	54	208	24	60	10
7.29	0.08	0.89	0.03	0.43	0.01	0.41	0.01	18.83	0.2	496	24	197	10	31	5
7.04	0.08	0.9	0.03	0.53	0.01	0.4	0.01	20.76	0.26	489	24	228	10	20	10
6.55	0.07	0.82	0.03	0.2	0.01	0.34	0.01	16.02	0.2	511	30	190	10	103	5
7.2	0.08	0.84	0.03	0.32	0.01	0.37	0.01	17.5	0.2	504	30	189	10	37	5
7.13	0.08	0.84	0.03	0.47	0.01	0.39	0.01	19.97	0.26	527	30	201	10	27	5
7.3	0.08	0.88	0.03	0.39	0.01	0.37	0.01	17.91	0.2	439	24	203	10	24	5
6.55	0.07	0.71	0.03	0.3	0.01	0.42	0.01	20.08	0.26	794	40	129	10	37	5
7	0.07	0.75	0.03	0.28	0.01	0.38	0.01	20.02	0.26	753	40	141	10	54	5
6.68	0.1	0.68	0.05	0.24	0.03	0.43	0.02	19.82	0.26	696	54	152	24	81	10
6.88	0.07	0.74	0.03	0.32	0.03	0.36	0.01	20.3	0.26	732	40	149	15	30	5
7.27	0.08	0.81	0.03	0.38	0.01	0.34	0.02	16.92	0.2	406	24	192	10	31	5
6.19	0.07	0.78	0.03	0.3	0.01	0.35	0.01	20.46	0.26	821	44	274	10	97	5
6.3	0.29	0.88	0.19	0.33	0.07	0.32	0.03	16.3	1.1						
6.93	0.32	1.03	0.12	0.41	0.06	0.37	0.02	18.8	1.2						

Bright, dust-bearing fine soils ratioed to dark soils at MER landing sites do not have the same patterns in enrichment and depletion as GB_A ratioed to GB_C, suggesting that the presence/absence of dust is not the key driver of compositional changes with grain size in Namib dune. A ratio of the Rocknest target Portage to GB_A is, however, similar to observed patterns for dusty MER soils (Figure 14b) (see also sections 4.3 and 4.4), implicating dust in Rocknest.

Variations in chemical composition measured by the ChemCam LIBS offer insight into whether the Bagnold sands are chemically homogenous or heterogeneous at the scale of the 300–550 μm ChemCam spot size. Because very few ≥500 μm sized particles exist in the Bagnold dunes (see section 3.1), ChemCam did not sample individual grains or mineral phases, but nevertheless, the small spot size allows identification of trends that indicate compositional variability in end-member constituent materials [see also *Cousin et al.*, 2017]. Principal component analyses of ChemCam LIBS data of Namib dune sands show that the chemistry of coarse fractions is variable and scattered, as expected if LIBS spots are mostly encountering only one to a few grains. On the other hand, samples with finer mean grain sizes vary between points enriched in Fe, Mg, and Al, typical of undisturbed and disturbed materials, and points enriched in silica, Ca, and/or having a low oxide total, typical for GB_A (Figure 15a).

Chemical data from most LIBS targets cluster together in the third and fourth principal components, pointing to the overall compositional homogeneity of the sands even when sampled at 300–550 μm scale, but outliers from the data cloud exist (Figure 15b). For example, relative to other soils, Husab (point 3) is enriched in Ca and depleted in Si, perhaps indicating anhydrite, and Doros (point 6) is enriched in Mg, Si, and Ti, perhaps indicating elevated pyroxene. Gobabeb C and D dump piles (points 4 and 9) have less Mg relative to Fe and Al.

Given the knowledge of the composition of the mineral end-members in CheMin data (section 3.3) [2017], the ChemCam composition data show trends consistent with the presence of mixtures of the specific mineral phases. In two-dimensional scatterplots, the strongest correlations are between Na
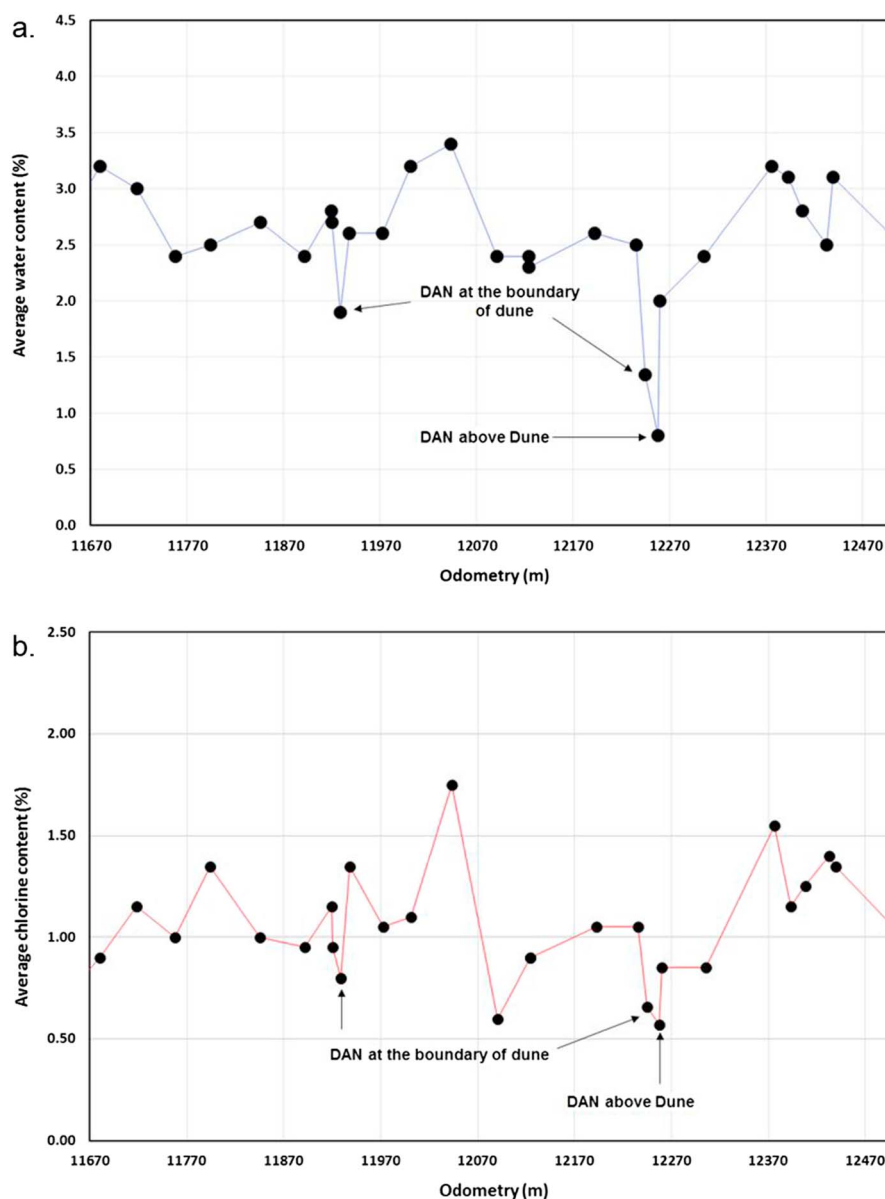
Figure 10. Modeled variation of (a) subsurface H_2O and (b) chlorine content of near-surface materials along the Curiosity traverse, derived from neutron measurements by the DAN instrument. The units in Figure 10a are reported water-equivalent hydrogen; no discrimination between H_2O and OH is implied. The units in Figure 10b are indicative of the Cl wt % present, but very large variations in other neutron absorbers like Fe, Ti, and Mn could modify chlorine-equivalent concentrations from the true concentration of chlorine by 5–10% (relative; formally, the axis is ξCl as in *Mitrafanov et al.* [2014] and *Litvak et al.*, 2016]).

and Al and Si, and the strongest anticorrelations are between Mg and Si; (Figure 16). Mafic and felsic minerals observed by CheMin are measured in different proportions by different LIBS points [see also *Cousin et al.*, 2017]. If the low oxide totals are a proxy for volatiles, both Fe and Si are correlated with volatile-enriched spots. GB_A is depleted in Mg, enriched in Fe, and has lower element totals but the same amount of Si relative to other Namib dune spots measured with LIBS (Figure 16). These chemical data are consistent with the results of CheMin analyses following a vigorous vibration in which some of the coarse material was removed from the analysis cell: in relative proportions of the remaining crystalline phases, mafic silicates were depleted and plagioclase, quartz, iron oxides, and anhydrite were enriched [*Achilles et al.*, 2017].
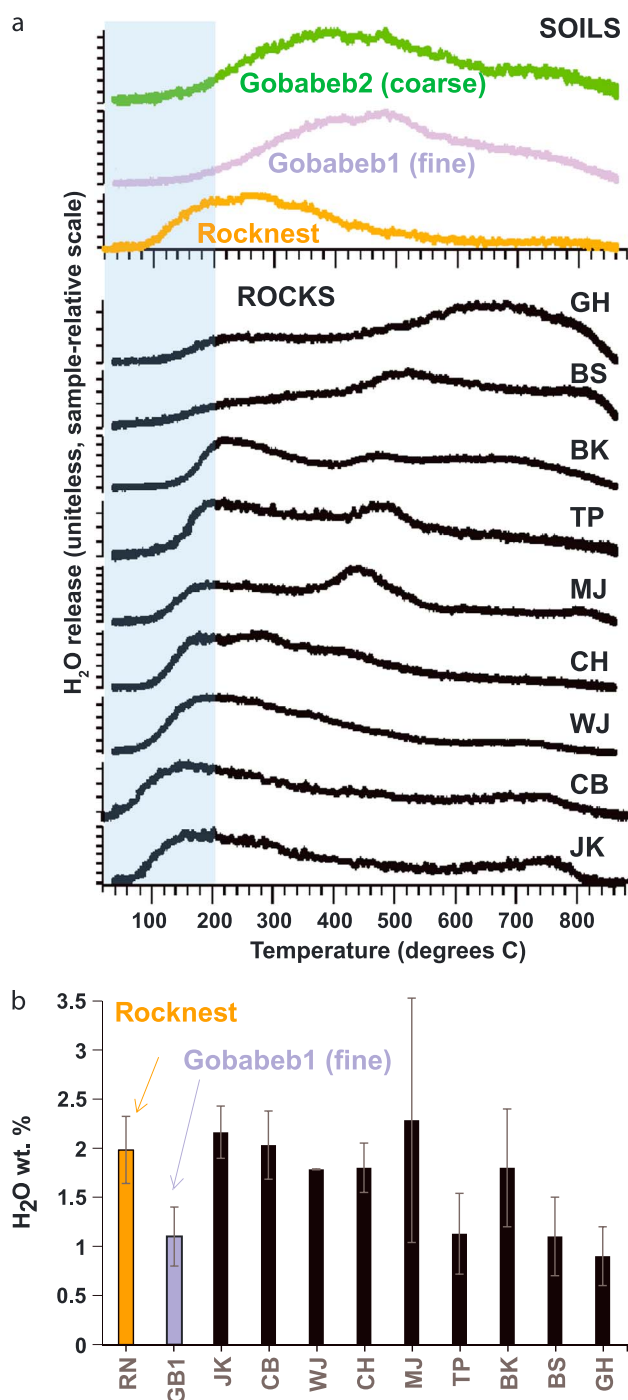
4. Discussion

4.1. Morphology of Particles, Size Distribution, and Comparison to Rocknest and MER Sites

The rounded to subrounded shapes of grains at the Bagnold dunes are consistent with attrition from extended periods of wind-driven saltation and reptation. As is typical for terrestrial dunes, the coarsest grains at both Namib and High dunes are commonly found along ripple crests. There are very few grains below MAHLI resolution ($<\sim$50 μm), and there are only a few large grains ($>$500 μm) (Figures 3–5 and Table 2) [*Cousin et al.*, 2017; *Edwards et al.*, 2017]. Sieved samples from GB_A (Figure 5) and undisturbed sands at Otavi [*Ewing et al.*, 2017; *Sullivan and Kok*, 2017] both have a modal grain size between 100 and 125 μm. Lack of coarse sand and larger grains is also suggested in ChemCam data by the fact that none of the single-point spectra yielded chemical compositions representative of single minerals, in contrast with measurements of some other Martian fines [*Cousin et al.*, 2017].

Because microscopic images can only examine small portions of the dunes, there is no single, representative Bagnold sand size frequency for comparison with other aeolian soils elsewhere on Mars. Nevertheless, all measured sand size frequencies at the Bagnold dunes had coarser modes than the ≤100 μm soil with subangular grains, documented at the Phoenix lander site by the Optical Microscope [*Goetz et al.*, 2010]. At the Gusev and Meridiani Planum MER sites, the science payload includes a Microscopic Imager (MI) [*Herkenhoff et al.*, 2003], capable of monochrome 31 μm/pixel images of soils and other targets. Namib dune sands are similar to but coarser than basaltic sands within Meridiani

Figure 11. SAM evolved gas analyses showing (a) the relative fraction of H_2O released as a function of temperature for the Gale crater sands and soils discussed in this work as well as rocks drilled, powdered, and measured to date and (b) the calculated weight percent H_2O for Gale crater soil and rock samples. The shaded region denotes release at <200°C, consistent with adsorbed or loosely bound water. All data in this figure are detailed in *Sutter et al.* [2017].

Planum's Eagle crater (50–200 μm and smaller), which are inferred to be active [*Soderblom et al.*, 2004; *Sullivan et al.*, 2005; *Weitz et al.*, 2006]. Mean grain sizes of Bangold dune targets are finer than ripples armored with 1–2 mm hematite concretions at Meridiani Planum, which are inferred to be inactive [*Sullivan et al.*, 2005;
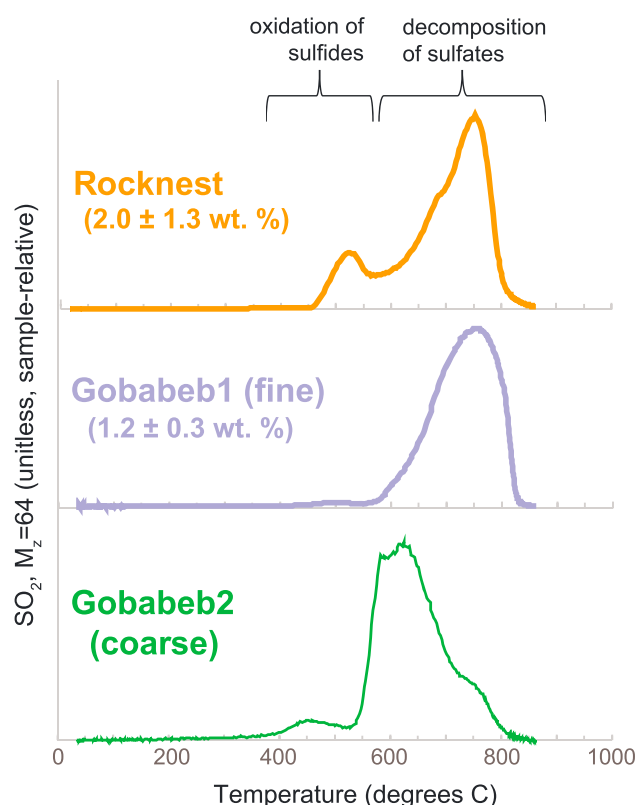
Figure 12. SAM evolved gas analyses of SO_2, showing release as a function of temperature for sand samples. Data and phase assignments are detailed in *Sutter et al.* [2017].

Jerolmack et al., 2006]. Over most of the Spirit rover traverse at Gusev crater, soils are poorly sorted and slightly cohesive [*Arvidson et al.*, 2004a, 2004b; *Cabrol et al.*, 2008, 2014; *Sullivan et al.*, 2008, 2011; *McGlynn et al.*, 2011]. The closest Gusev analog to any sands measured in the Bagnold dune field is at El Dorado, an ~0.04 km^2 ripple field, where a thin layer of well-rounded, well-sorted 200–300 μm grains mantles mostly ≤100 μm grains in the near subsurface [*Sullivan et al.*, 2008]. This size variation is similar to but more pronounced than surface-subsurface differences observed near High dune in Gale (Figure 3). Namib dune has no such difference in grain size between the interior and exterior, at least within the upper ~20 cm accessed by the wheel scuff.

Importantly, the sands examined at Namib and High dunes differ from aeolian materials investigated at the dust-covered, inactive Rocknest bedform, 7 km away and well outside the Bagnold dune field [*Blake et al.*, 2013; *Leshin et al.*, 2013; *Minitti et al.*, 2013] (Figure 17). In addition to the presence of surface dust, the Rocknest bedform grain size frequency is bimodal, with a slightly cohesive thin surface crust of coarse and very coarse sand overlying a cohesive interior of much finer grains with a large proportion below MAHLI resolution [*Minitti et al.*, 2013]. The reddish hue of these materials exposed by a wheel scuff suggests the presence of mixed-in air fall dust—unlike subsurface materials exposed by wheel motions at Namib and High dunes. The highest-resolution MAHLI views at Namib and High dunes show little evidence for grains ≤50 μm and indicate that sands are cohesionless or nearly so and tend to be less red. Overall, there is little or no evidence for dust in the MAHLI images of the Bagnold sands. Collectively, observations of the Bagnold sands at Namib and High dunes are consistent with observations made from orbit and from the ground of sand transport and bedform motion, i.e., present-day wind-driven activity [*Silvestro et al.*, 2016; *Bridges et al.*, 2012, 2017; *Lapotre et al.*, 2017, *Sullivan and Kok*, 2017].

4.2. Composition and Evidence for Compositional Variation With Grain Size

Phoenix optical microscope images produced the first microscopic color data for Mars soils, revealing at least four color types (reddish and white fines and brown and black sands), present at the Phoenix size [*Goetz et al.*, 2010]. MAHLI images of Bagnold dune sands also reveal visible-wavelength color properties that vary substantially between grains, indicating that the particles are derived from diverse lithologic units and/or that parent rocks have broken down into constituent mineral grains. Four color classes commonly occur in the Bagnold dunes (Figure 5). Gray opaque grains comprise at least 50% of the samples. They do not obviously correspond to one of the four most abundant CheMin minerals but could be basaltic lithic or glassy fragments. Translucent yellow grains are likely monomineralic and could be either Ca,Na-feldspar with a small amount of Fe, high-Ca pyroxene, or medium-Fo# olivine; i.e., the color observed corresponds with multiple minerals measured by CheMin. The reddish grains vary substantially in hue and could represent weathered basaltic lithologies (e.g., oxidatively weathered gray grains) or sand-sized clasts of Murray formation rock
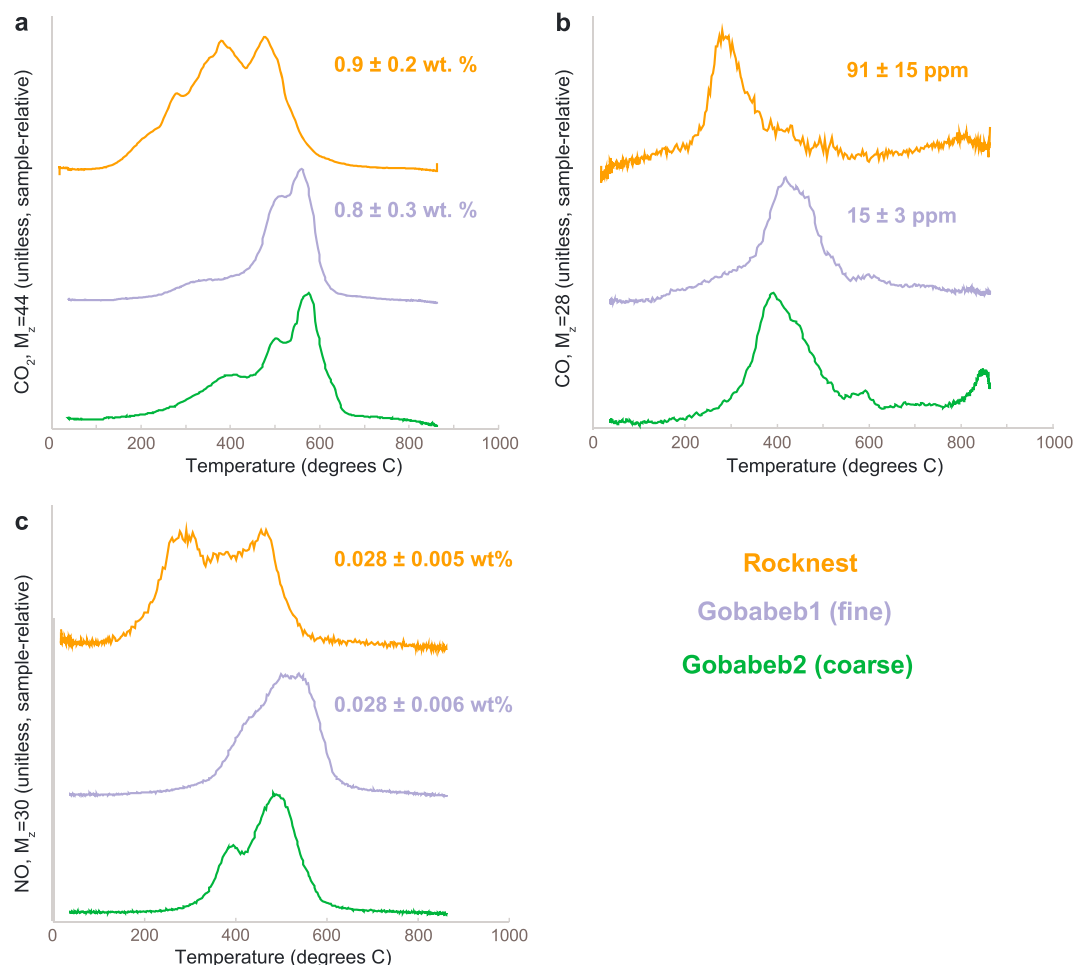
Figure 13. SAM evolved gas analyses of (a) CO_2 (corrected for MTBSTFA), (b) CO, and (c) NO, showing release as a function of temperature for sand samples. Data are detailed in *Sutter et al.* [2017].

but do not correspond with a specific mineral identified by CheMin. Rare green grains (Figure 4d) could be a low-Ca pyroxene or high Fo# olivine, different from the medium Fo# of the bulk sample. Regardless of the specific color assignments to phases or lithologies, greater proportions of gray opaque grains and decreasing numbers of reddish grains are observed in coarser fractions.

Sands change in composition as a function of mean grain size. Gobabeb discard piles with mean grain sizes >150 μm are significantly enriched in Mg, Ni, modestly enriched in Fe and Mn, depleted in major oxides other than SiO_2, and modestly depleted in S and Cl relative to finer grained samples (Figure 14) [see also *O'Connell-Cooper et al.*, 2017; *Cousin et al.*, 2017]. This indicates compositional differences caused by size segregation and the enrichment of olivine and/or pyroxene in the coarsest fraction, in agreement with spectroscopic data [*Johnson et al.*, 2017]. Consequently, CheMin data measured on the <150 μm fraction are only a lower bound on the quantities of mafic minerals in the Bagnold dunes. Nonetheless, the patterns of evolved volatiles as a function of temperature are similar for both the Gobabeb coarse and the fine fraction with the exception of SO_2 and NO (Figures 11–13). In particular, SAM data for SO_2 show slightly different decomposition temperatures, inferred to result from differences in the sulfate cation, and a low temperature SO_2 release unique to the coarse fraction, which indicates the existence of sulfides (Figure 12) [*Sutter et al.*, 2017].

Compositional outliers within the Bagnold sample set are related primarily to physical sorting processes, which relate to the activity (or inactivity) of the bedforms and drive grain size differences. In contrast to the samples examined at Namib dune, the samples examined near High dune contain some very fine grained reddish particles, especially within Weissrand disturbed sands, Kibnas trough sand, and the interstices of
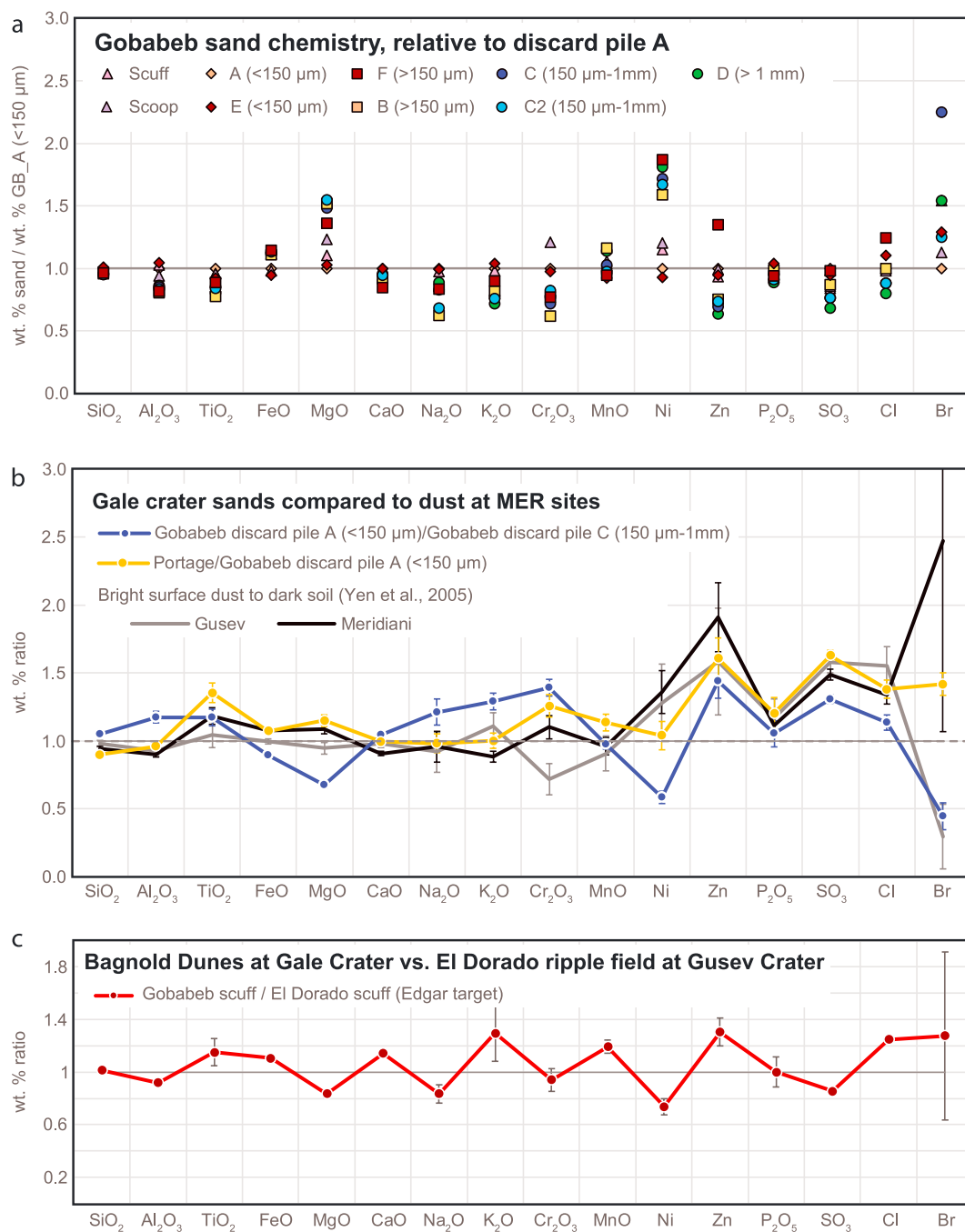
Figure 14. (a) Ratio of the chemical composition of Gobabeb APXS measurements to Gobabeb pile A, the <150 μm sample ingested into CheMin and SAM. Note that samples E and F may be somewhat influenced by the underlying substrate, a sedimentary rock. (b) Select ratios of fine to coarse soil samples, including Gale crater's Gobabeb_pileA (<150 μm)/Gobabeb_pileC (150 μm to 1 mm) and Rocknest_Portage/Gobabeb pile A compared to the ratios of bright surface dust to dark soil from Meridiani Planum and Gusev crater, measured by the MER rovers [*Yen et al.*, 2005]. (c) Ratio of the scuff at Gobabeb, Namib Dunes, and Gale crater to the scuff Edgar, in the El Dorado ripple field at Gusev crater (data from *Ming et al.* [2008]).

larger particles on the ripple Warsaw, which may migrate infrequently due to their large grain size. That the sand patch near High dune is brighter and redder than Namib dune in VNIR spectral data [*Johnson et al.*, 2017] is consistent with the presence of these grains. There are subtle color differences between the surface and near surface at Namib that might indicate minor surface dust at Gobabeb (Figure 6), but overall, Namib
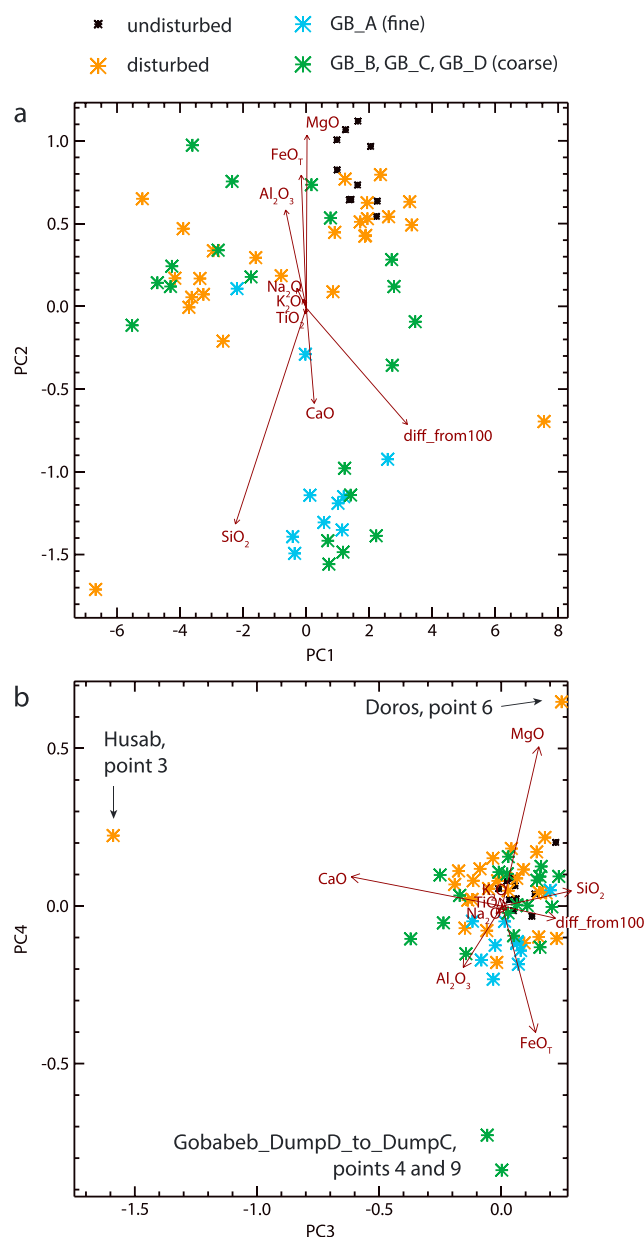
Figure 15. Principal component analysis biplots of ChemCam of Namib Dune targets (excluding the nighttime data from GB_A) with oxides contributing to each factor indicated for (a) principal components 1 and 2 and (b) principal components 3 and 4. Methodology is the same as in Figure 9. Sands are color coded for undisturbed (Dwyka), disturbed (Doros, Husab, Gosser_Scuff), the fine fraction of sieved materials (<150 um; GB_A), and the coarse fractions of sieved materials (GB_B, GB_C, GB_D). "Diff_from_100" is the difference in the oxide weight percent totals from 100%, a proxy for volatiles and/or minor elements.

materials are considerably more homogeneous in color and grain size than at High dune, than observed at Rocknest [*Minitti et al.*, 2013], or within dark-toned aeolian sands at prior landing sites [e.g., *Sullivan et al.*, 2008]. The activity of Namib dune appears to be responsible for its lack of silt-sized and smaller grains, vertical homogeneity in grain size and chemistry, and distinctive spectral properties.

4.3. Volatile Concentration in Fine Fraction of Martian Soils

Perhaps the most striking aspect of the composition of the dunes is their distinctive volatile content. Cross-instrument consideration of H_2O, Cl, and S with ChemCam, APXS, SAM, and DAN shows that the dunes are substantially depleted in these volatiles and enriched in silicate minerals relative to all targets measured so far at Gale crater (Figures 9 and 10). This is consistent with the lack of crystalline CheMin-measured hydrous phases in the dunes, in contrast to drilled sedimentary rock samples, which contain crystalline hydrated or hydroxylated minerals (primarily clay minerals and silica phases). The H_2O, Cl, and S contents of Bagnold dune sands are also significantly less than that measured in Rocknest, the other soil target sampled for analyses by SAM and CheMin. The 1.5–3 wt % water release at Rocknest included a substantial component of adsorbed water (release at $T < \sim200°C$ of $\sim15–20\%$). In contrast, over 90% of the ~1 wt % H_2O in Gobabeb samples evolved between 200 and 800°C (Figure 14), consistent with loss mostly from hydroxylated phases or fluid inclusions.

Multiple hypotheses could explain the atypically low abundance of H_2O, Cl, and S the Bagnold sands: abrasion and removal of alteration coatings on sand grains by collisions during saltation [e.g., *Cousin et al.*, 2015], less weathered materials in the sand fraction (thus also implying a volatile poor, relatively unaltered amorphous phase) [*Cousin et al.*, 2017], or fewer fine-grained particles. Considering collectively the spectral properties of the sands, grain size analyses from MAHLI images, and elemental data, we favor the hypothesis that the paucity of volatiles in the Bagnold dunes results from a lack of dust- and silt-sized particles, especially at active Namib. That is, the dust and/or silt fractions—by virtue of either their
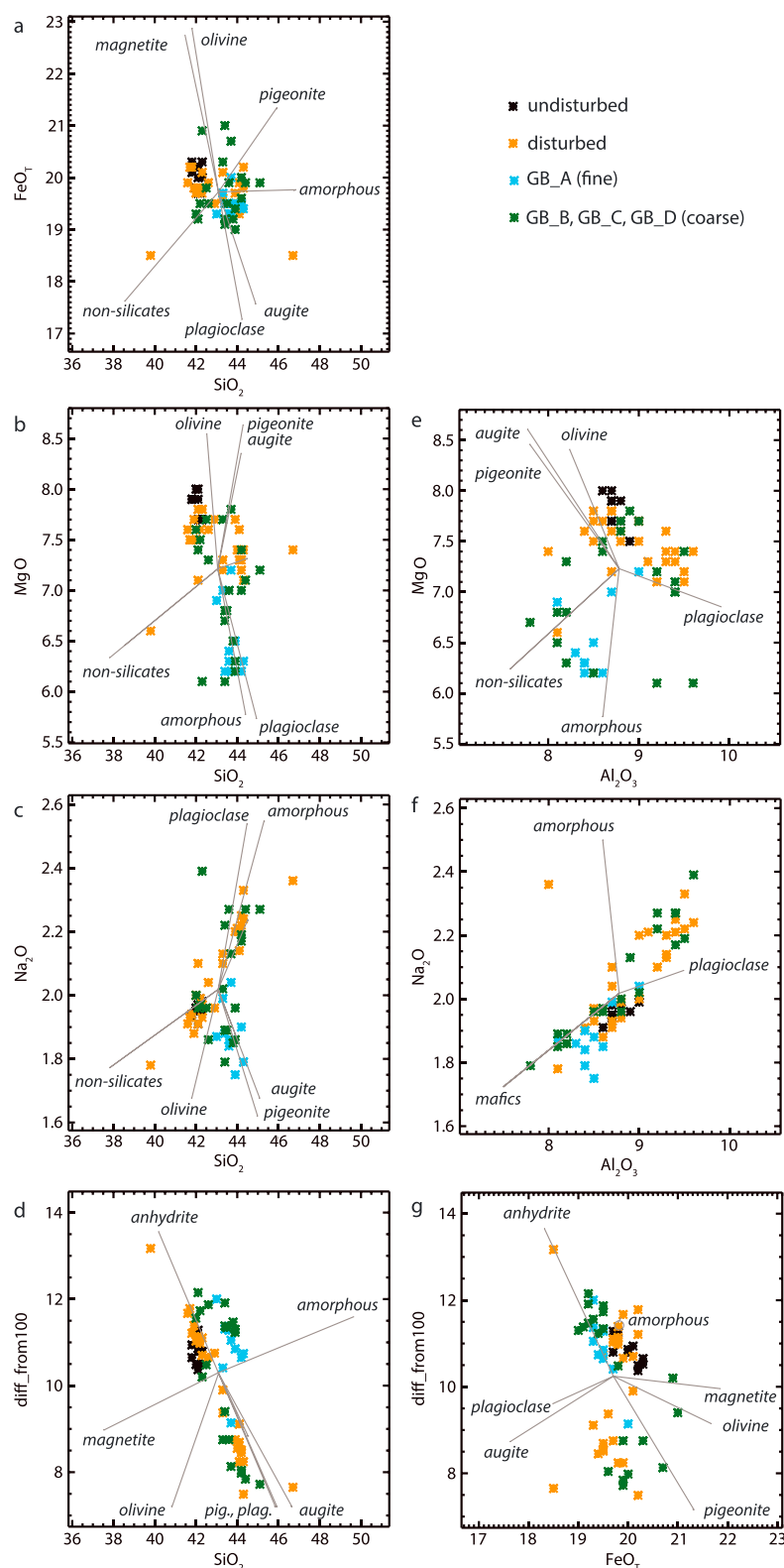
Figure 16. Scatterplots illustrating relationships between elements as measured at the Namib dune by the ChemCam LIBS instrument. The centroid is the average ChemCam-determined elemental composition, and lines radiate outward in the direction of end-member crystalline phases or the amorphous phase as determined by CheMin [*Achilles et al.*, 2017]. (a) FeO versus SiO_2, (b) MgO versus SiO_2, (c) Na_2O versus SiO_2, (d) element total difference from 100 wt % versus SiO_2, (e) MgO versus Al_2O_3, (f) Na_2O versus Al_2O_3, and (g) element total difference from 100 wt % versus FeO.
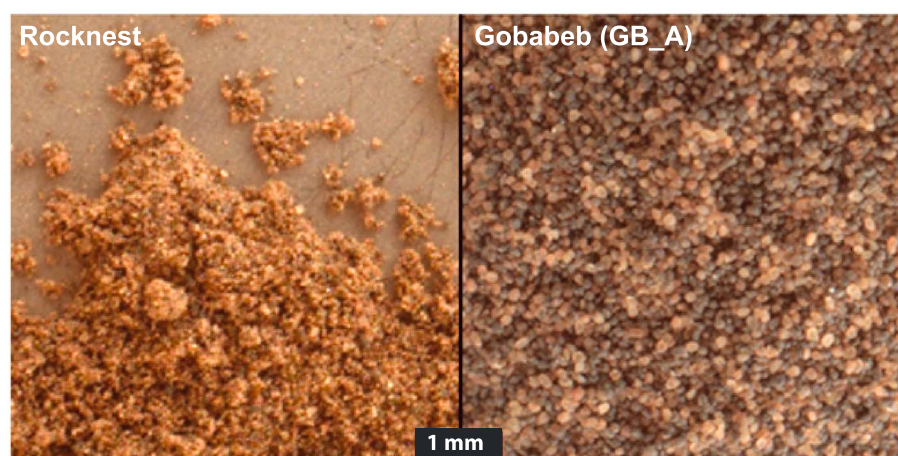
Figure 17. Comparison of grain size of the <150 μm sieved samples from the (left) Rocknest bedform and (right) Namib Dune. The <150 μm sieved fraction from Rocknest Scoop 5 was deposited on the rover's observation tray (portion of MAHLI image 0095MH0001310010101121C00; resolution ~21.1 μm/pixel). The <150 μm sieved fraction from Gobabeb Scoop 1 was deposited in discard pile A (portion of MAHLI image 1228MH0005630010403429C00; resolution ~16.7 μm/pixel, displayed reduced by 79.1% so as to be at the same scale as the Rocknest sample). Both images were acquired with the target materials fully shadowed by arm/turret hardware, then dynamic range stretched, and sharpened.

chemical/mineral phases or by virtue of their high specific surface area—are the major carrier(s) of water, S, and Cl in the Martian soils.

This interpretation is consistent with ChemCam data showing H, associated with the finest-grained and lowest-SiO_2 component in the first 250 sols of the mission [*Meslin et al.*, 2013; *Cousin et al.*, 2015]. This interpretation is also supported by chemical differences between Rocknest and Gobabeb that are similar to differences between dusty and nondusty soils measured by MER (Figure 14b). S and Cl have long been recognized as enriched in Martian fines [*Clark and Baird*, 1979; *Yen et al.*, 2005; *Berger et al.*, 2016] but are depleted (along with Zn, another dust component [*Yen et al.*, 2005]) in the Bagnold sites investigated. The greater H_2O in Rocknest could be associated with Cl- or S-associated salts (e.g., hydrous salts) or be within poorly crystalline oxide or silicate alteration products also within the fine fraction.

The finding that the size fraction <~45 μm is a—and perhaps *the*—major carrier of water in Martian surface fines has implications for evaluation of the in situ resource utilization potential of soils, e.g., the harvesting of water from Martian fines for use in human exploration. Dust and silt collection and processing at moderate temperature may be a fruitful avenue for water extraction because of the ubiquity of Mars soils and the ability to isolate and concentrate the finest fraction by a simple procedure like sieving.

4.4. Evidence for Two Distinct Amorphous Components in Martian Soils

Even though the Gobabeb sands are volatile poor, they are not volatile free, and there is a carrier of the volatiles within the sand-sized fraction. SAM data show that CO_2 and NO release from the <150 μm fraction (GB1; equivalent to GB_A) is, along with Rocknest, among the highest at Gale crater [*Sutter et al.*, 2017]. SAM EGA release profiles indicate sulfates and carbonates [*Sutter et al.*, 2017], which are likely poorly crystalline or present in abundances <1–2 wt % due to their nondetection by CheMin. The H_2O present in the GB1 sample must reside mostly in an XRD-amorphous component(s) because CheMin did not identify crystalline phases with structural water or hydroxyls to accommodate the ~1 wt % water.

The combined use of derived CheMin crystal chemistry with bulk APXS data from the <150 μm sample permits estimation of the composition of the Gobabeb sands amorphous phase(s) (Table 4) [see also 2017]. There are several caveats. Using the average estimate of 35 wt % amorphous, the estimated chemical composition would be −3% MgO. Thus, the quantity of the amorphous phase(s) is >41 wt % or there is some uncertainty in the composition of the olivine and/or pyroxenes (see *Achilles et al.* [2017] for a more detailed discussion of uncertainties in computation of the amorphous phase(s)). Nevertheless, regardless of the exact quantity used in the calculation, the XRD-amorphous phase(s) in the dune sands at Gobabeb are composed primarily of Si, Fe, Al, and volatiles. The Gobabeb amorphous phase(s) have slightly more Si and Fe but less Al

Table 4. Chemical Compositions, Measured and Derived, for Crystalline and Amorphous Fractions in Gobabeb (GB) and Rocknest (RN)

	Weight Percent of Sample	SiO2	TiO2	Al2O3	FeO	MgO	CaO	Na2O	K2O	SO3	P2O5	Cl	Cr2O3	MnO	Total
Measured or Directly Derived Sample Composition															
APXS_GB_GB_A	100%	47.9	0.9	9.8	17.9	7.6	7.3	2.8	0.5	3.4	0.8	0.5	0.4	0.4	100
APXS_RN_PORTAGE	100%	43.0	1.1	9.4	19.2	8.7	7.3	2.7	0.5	5.5	1.0	0.7	0.5	0.4	100
CheMin_GB_xII_only[a]	(100% -amorphous %)	46.6	0.0	11.1	16.5	12.9	10.2	1.5	0.0	0.8	0.0	0.0	0.0	0.0	100
CheMin_RN_xII_only[a]	(100% -amorphous %)	47.6	0.7	11.5	17.0	11.3	8.8	2.3	0.0	0.8	0.0	0.0	0.0	0.0	100
APXS_Dust_Berger_sol571	100%	39.3	1.1	8.9	21.0	8.3	7.0	2.8	0.5	8.3	n.a.	1.1	n.a.	0.4	98.7
Amorphous Fraction Composition Estimates[b]															
Bulk_Amph_GB_15pct	15 wt % of APXS_GB_A	55.0	5.9	2.1	25.7	−22.7	−9.0	9.6	3.3	18.1	5.3	3.3	2.6	2.5	101.7
Bulk_Amph_GB_50pct	50 wt % of APXS_GB_A	49.1	1.8	8.4	19.3	2.2	4.4	4.0	1.0	6.0	1.6	1.0	0.8	0.7	100.3
Bulk_Amph_GB_Achilles	41 wt % of APXS_GB_A	49.6	2.1	7.9	19.6	0.0	3.2	4.5	1.2	7.1	1.9	1.2	0.9	0.9	100
Bulk_Amph_RN_Achilles	~35 wt % of APXS_Portage	30.4	2.6	3.9	25.4	1.7	3.4	3.8	1.8	18.0	3.5	2.3	1.8	1.5	100
Distinct Amorphous Reservoirs, Composition Estimates															
Amph_Dust_only[c]	36–41 wt % of APXS_Dust_Berger_sol571	26.0	3.0	4.9	29.0	0.0	1.4	4.9	1.3	22.0	n.a.	3.0	n.a.	1.2	96.7
Amph_GB_not_dust_95pct	95[d] wt % of Bulk_Amph_GB_Achilles	50.9	2.1	8.0	19.4	0.0	3.3	4.4	1.2	6.2	2.0	1.1	1.0	0.9	100.6
Amph_GB_not_dust_68pct	68[d] wt % of Bulk_Amph_GB_Achilles	60.8	1.7	9.3	15.6	0.0	4.1	4.2	1.1	0.0	2.8	0.4	1.4	0.8	102.1
Consistency Check Using Derived Amorphous Endmembers to Compute the RN Amorphous Phase															
Bulk_Amph_RN_computed[e]		32.3	2.7	5.7	26.6	0.0	1.9	4.8	1.3	18.0	n.a.	2.5	n.a.	1.1	96.9
difference from actual		1.8	0.2	1.8	1.2	−1.7	−1.5	1.0	−0.5	0.0	n.a.	0.3	n.a.	−0.4	n/a

[a]Calculated from *Achilles et al.*, 2017 from proportions of crystalline minerals whose unit cell parameters were determined by Rietveld refinement.
[b]Multiple estimates of the bulk amorphous fraction composition: The estimates with Bulk_Amph_GB_Xpct are from this work and use the lower and upper bounds of the *Achilles et al.*, 2017 estimates of the XRD-amorphous/nondetectable fraction (15 wt % and 50 wt %). The preferred value of 41.4 wt %, used in further computations, is the minimum required such that the Mg content is nonnegative and is nearly identical to the value derived by 2017. Amph_RN_Achilles is the bulk amorphous fraction composition from the Rocknest sample [*Achilles et al.*, 2017 *Morrison et al.*, 2017a, 2017b].
[c]The composition of the amorphous component due to dust is computed from the sol 571 dust measurement by *Berger et al.* [2016], assuming that bulk dust is composed of an amorphous fraction and a crystalline fraction (assumed to be CheMin_GB_xII_only, absent other data on silicate proportions). The proportion of the crystalline component was estimated to be 64.3% by adjusting the proportion until the MgO content of the amorphous phase became zero, as no MgO was estimated for the Gobabeb amorphous fraction. Were Mg contents of up to 1.7 wt % MgO permitted, as in the Rocknest sample, the value would be 59 wt % crystalline.
[d]A range of compositions for the nondust-related amorphous component were computed assuming values of the amorphous fraction due to dust ranging from 5 wt % to 32 wt %. SO3 content becomes negative for values higher than 32 wt %. MAHLI data support 5 wt % dust as the preferred value due to lack of small grains.
[e]The minimum absolute value of the sum of the differences in oxide weight percent between modeled and estimated Bulk_Amph_RN_Achilles is 10.4 wt % and occurs at 75 wt % of the Rocknest amorphous fraction due to dust, if 5 wt % of the Gobabeb amorphous fraction is assumed to be dust, and 82 wt % dust, if 32 wt % of the Gobabeb amorphous fraction is assumed to be dust.

than the weighted sum of the crystalline sample (Table 4 and Figure 18). All water released is at relatively high temperatures (>150°C with most >400°C; Figure 11). Speculatively, given an inferred amorphous composition similar to the crystalline phases, this amorphous component could simply represent the poorly crystalline, hydroxylated alteration products of pyroxenes, olivines, and feldspars, i.e., amorphous products with chemistries similar to phyllosilicates and iron oxides. This has been observed in terrestrial settings for pyroxene partially altered to serpentine, where chemical bonds characteristic of the serpentine mineral structure can be seen in infrared data but are too short order for XRD detection and comprise an amorphous component [*Leask and Ehlmann*, 2016]. Alternatively, Si-enriched volcanic or impact glasses that are hydroxylated or have H_2O-bearing inclusions could also explain the high-temperature evolved water. Derivation of the silica-enriched amorphous phase from nearby silica-enriched portions of Murray formation bedrock is not favored because many of the Murray silica phases are crystalline [e.g., *Morris et al.*, 2016] and would be XRD detectable.

The nanophase ferric oxide component from Mössbauer analysis of dusty MER soils correlates with both Cl and S [e.g., *Yen et al.*, 2005; *Morris et al.*, 2006a, 2006b]. Fe and hydration enrichment was observed previously in fine soils, including Rocknest, analyzed by ChemCam [*Meslin et al.*, 2013]. Here we suggest that the low-temperature H_2O release in Rocknest (but not present in Gobabeb) is associated with a Fe-rich amorphous component, which is likely a ferrihydrite-, schwertmanite-, and/or akaganeite-like phase specific to the silt- and dust-sized fraction. Rocknest amorphous phase(s) are Si and Al poor relative to the amorphous compositions calculated for Gobabeb from combined APXS and CheMin analyses [*Dehouck et al.*, 2014; *Achilles et al.*, 2017; *Morrison et al.*, 2017a, 2017b]. Adopting a different approach to isolate the amorphous phase in dust specifically, we estimate the amorphous phase composition in dust using a measured bulk dust composition [*Berger et al.*, 2016], and subtracting crystalline phases present the same proportions as in the Gobabeb sands until the Mg is accounted for (Table 4). Dust has both crystalline and noncrystalline components [*Goetz et al.*, 2005;
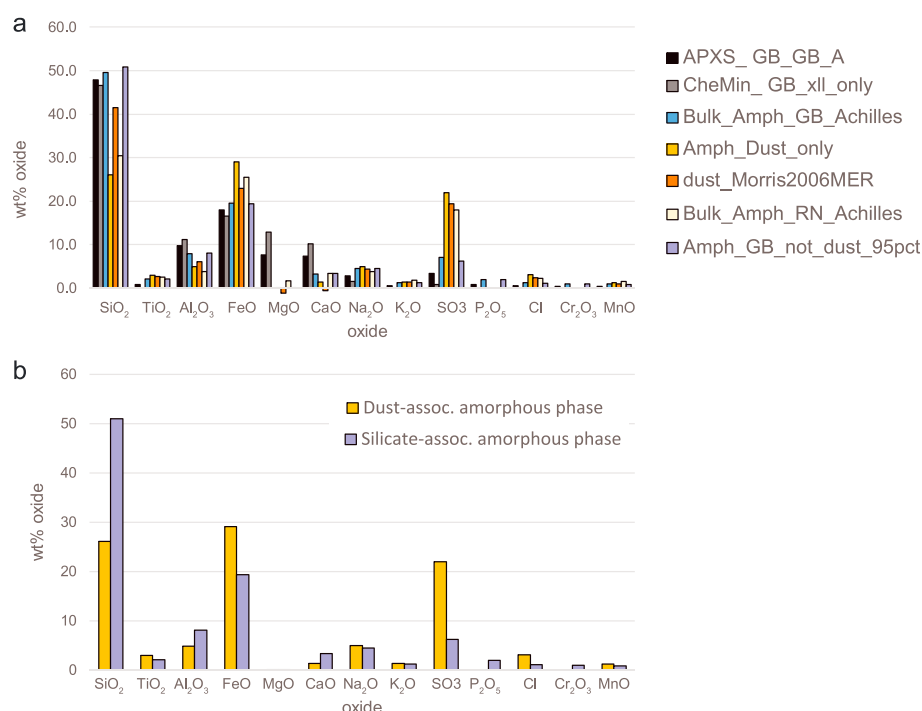
Figure 18. Chemical compositions from Table 4 and estimates of dust composition by *Morris et al*. [2006a, 2006b] from MER data with (a) the composition of multiple measured and derived quantities and (b) estimates of the chemistry of only the two amorphous phases.

Hamilton et al., 2005; *Morris et al*., 2006a, 2006b]. The assumption that the phases are approximately in equal proportions is justified by their similarity in Gale soils separated by kilometers. This procedure estimates that the dust is 64% crystalline and 36% amorphous, a value similar to the partitioning of Fe between crystalline (55%) and nanophase (45%) iron-bearing phases calculated from Moessbauer data from MER [*Goetz et al*., 2005]. The dust-related amorphous phase is Si poor and Fe enriched and must host several weight percent of both adsorbed and mineral bound water, as well as S, Cl, and Zn (Table 4 and Figure 18). Using this calculated dust-related amorphous phase, ~75–82% of the amorphous material in Rocknest is due to contribution of the amorphous components of dust (Table 4), a proportion similar to the ~75% of fine materials in the Rocknest aeolian bedform that were too small to resolve in the acquired MAHLI data [*Minitti et al*., 2013]. By the same constraint, the dust must be <32 wt % for Gobabeb and MAHLI data suggest that it is considerably less (<5%).

Thus, differences in the water and volatile contents of the Rocknest and Gobabeb soils are not merely due to the greater surface area available for adsorbed water in fine materials but rather to distinctive chemical hosts in the amorphous fraction that vary with size. Collectively, the sieved and size-controlled coordinated measurements of Martian sands and soils point to two discrete reservoirs of volatiles in Martian fines (Figure 18): (1) an Si-enriched amorphous component associated with sand-sized silicate, which derives from partially hydroxlated products of alteration, bound water/OH in glasses, or both, and (2) an Fe-, S-, and Cl-enriched and Si-poor amorphous component in dust and silts <50 μm in size with adsorbed and more loosely bound water. This conclusion is consistent with the conclusions of *Leshin et al*. [2013], *Meslin et al*. [2013], and *Cousin et al*. [2015] regarding the volatile enrichment of the amorphous component. The natural wind sorting-induced size fraction at Bagnold permitted the discovery of two distinct, grain size-dependent volatile reservoirs.

4.5. Source Rock(s) and Relationship to Gale Crater Sedimentary Rocks

Gale crater was once a net sediment sink; after its formation in the late Noachian/early Hesperian, materials deposited in the crater became buried and lithified. Later, conditions changed such that Gale became a net sediment source, and much of the basin deepened again, due to differential weathering and wind erosion of

reexposed rocks. *Thomson et al.* [2011] suggested that the bulk of these events largely occurred during a roughly 200–500 Ma period after Gale crater formed. Erosional unconformities in Gale's rock record suggest that some aspects of this process of filling or partial filling, lithification, and exhumation may have occurred more than once [*Malin and Edgett*, 2000; *Anderson and Bell*, 2010; *Fraeman et al.*, 2016; *Buz et al.*, 2017]. The last recent period of deposition appears to be late Hesperian or Amazonian, but erosion has dominated for at least the last 1 Ga [*Pelkey et al.*, 2004; *Grant et al.*, 2014; *Ehlmann and Buz*, 2015]. Today, disaggregated clastic materials likely leave the basin [*Day and Kocurek*, 2016], e.g., as indicated by a low-albedo wind streak extending southward from Gale [e.g., *Anderson and Bell*, 2010].

Thus, the most likely source for Bagnold dune sands would be sand-bearing sedimentary rocks within Gale, exposed and undergoing weathering and erosion. These include the sandy matrix of fluvial-alluvial conglomerates described by *Williams et al.* [2013] (in the Bradbury group), the fluvial and deltaic sandstones described by *Grotzinger et al.* [2015] (in the Bradbury group), the aeolian Stimson sandstones described by *Banham et al.* [2017] (in the Siccar Point group), and perhaps sand-sized lithic fragments, vein mineral fragments, and concretions that might weather out of any of the sedimentary rocks [*Grotzinger et al.*, 2014, 2015], observed during the MSL mission as of sol 1600. We compared the bulk chemical composition of Bagnold samples from Namib dune with sandstones interbedded with finer lacustrine facies in the Bradbury group (Aeolis Palus) and with Stimson formation sandstones within the Siccar Point group (Figures 1 and 19 and Table 5). Among the potential sandstone source rocks, Bagnold sands are more similar to the Stimson sandstones than Bradbury sandstones, but there are also key differences (Figure 19 and Table 5). Na, Al, Ti, Zn, P, and Cr are notably lower and Ni and Mg notably higher in the Bagnold dunes relative to Stimson (Figure 19).

Thus, ongoing erosion of Stimson sandstones may contribute to the production of the Bagnold dunes. Yet the compositional data do not necessitate a Bagnold sand origin from Stimson, and, indeed, the compositional differences highlight the importance of physical or chemical alteration of the sandstones and/or additional sources. If the Stimson were the principal contributor, a physical weathering process would be required to remove the dust-associated elements and enrich some mafics (Ni and Mg carriers). Winnowing of finer dust and silt particles by removal is straightforward as these are removed in suspension during self-organization of the dunes. However, in contrast to Gobabeb sands, the Stimson sandstones contain no olivine above the 1–2 wt % threshold of CheMin detection [*Yen et al.*, 2017]. There is no modern evidence for regional sands blowing into Gale, so sand-sized grains eroded from the olivine-bearing Gale walls [e.g., *Ehlmann and Buz*, 2015; *Buz et al.*, 2017], sandstones exposed elsewhere on the Gale floor [e.g., *Buz et al.*, 2017], or sandstone strata further up Mount Sharp than the rover has traversed [e.g., *Le Deit et al.*, 2013] are the most likely sources of mafics.

A second key question is whether the Bagnold dunes are a modern chemical or mineralogical analog for ancient sandstones. The Bagnold dunes are sufficiently chemically different from the fluvial/deltaic sandstones of Bradbury (e.g., Shaler sandstone [*Anderson et al.*, 2015]) (for others, see *Siebach et al.* [2017]) that they are likely not similar to Bradbury's starting protolith. Removal of Ca, Si, Ni, Na, and Al and addition of Zn, K, Fe, Mn, Ti, Cr, and salt anions would be required for Bagnold sands to make Bradbury materials. Some of these (salt anions, K, Fe, and Zn) might plausibly be explained by the action of diagenetic fluids. The others would seem to require physical intermixtures of materials from other sources. On the other hand, the Stimson sandstones are simpler to reproduce from Bagnold sands by intermixture of elements associated with dust as the bedforms become inactive and size sorting that favors the fine fraction over the coarse fraction. The compositional differences between Stimson and the Namib dune average (Figure 19) are similar to the relative compositional differences in the discard pile A sample (<150 μm) versus the coarser fractions (>150 μm) (Figure 14). Additional extensive, open system diagenetic alteration need not be invoked to explain the chemistry, though some closed-system alteration would be required to alter the olivine. The enrichment of Cl, Br, and S in sandstones relative to the dune sands may point to their alteration by fluids, either syndepositionally (e.g., an evaporating playa lake) or postdepositionally (e.g., by diagenetic fluids).

4.6. Implications for Martian Sediment Transport: Global Versus Local

A final question is to what extent Martian sands and soils are globally derived versus representative of local lithologies. The relative ease of entrainment of sand grains, their survival due to low kinetic energies of impact for the < ~300 μm fraction, and long saltation hop distances enable regional and possibly global mixing [e.g., *Sullivan et al.*, 2014]. Impact cratering may further promote mixing. Nonetheless, sands from Gusev
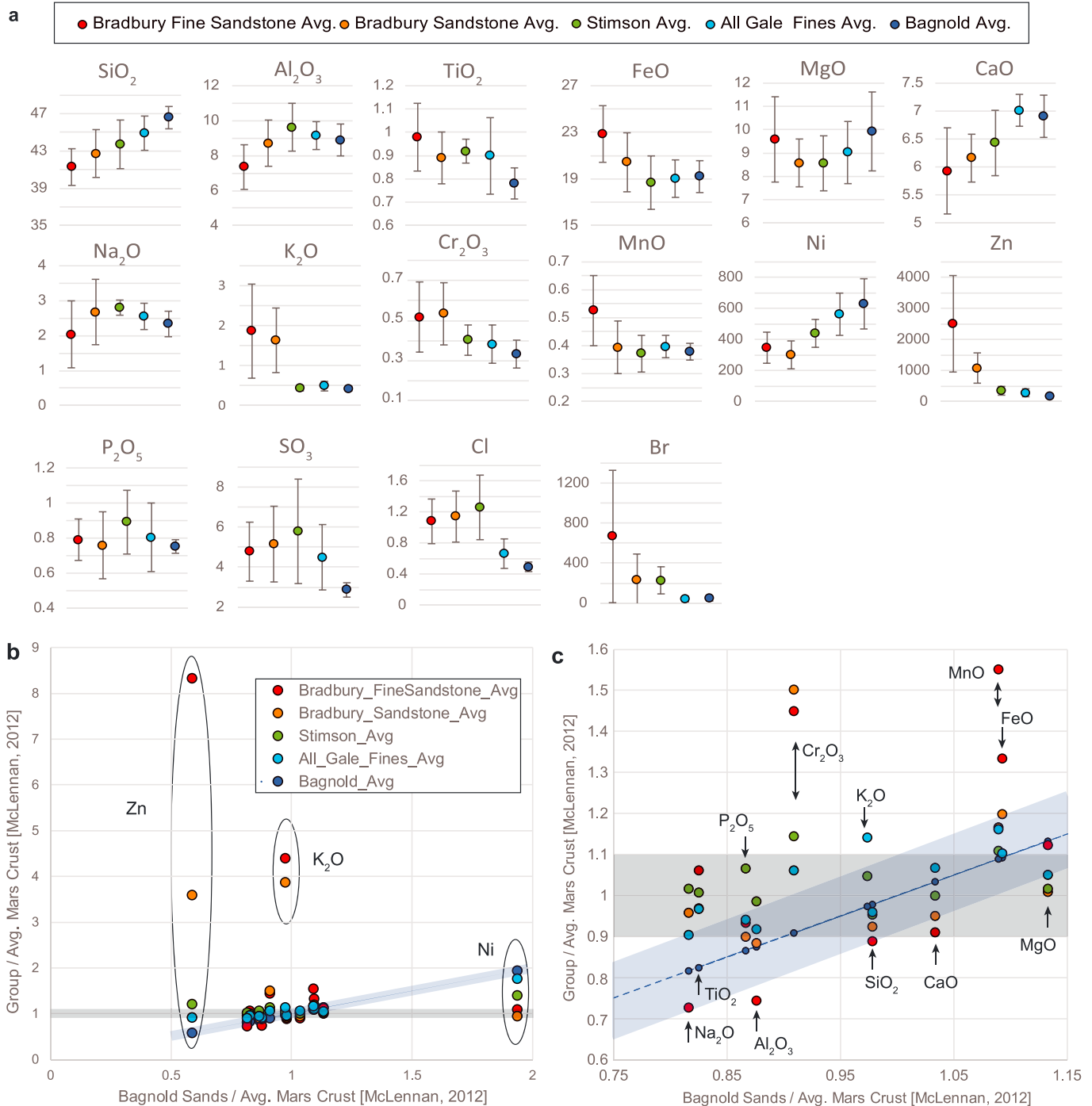
Figure 19. Bagnold dune composition at active Namib, measured by APXS, and compared to other groups of materials with sand-sized grains (Table 5): fine sandstones and sandstones of the Bradbury Group (Aeolis Palus), sandstones of the Stimson formation, and all Gale crater fine-grained materials (including the Bagnold sands). Sandstone rock data are from *Siebach et al.* [2017]. (a) Each point is the group average for the oxide or element, and error bars indicate standard deviation of data. The *y* axis is in weight percent except for Ni, Zn, and Br, which are in ppm. (b) The groups from Figure 19a were then ratioed to the estimated Mars crust composition from *McLennan* [2012] to normalize data for plotting. The ratio for each group was then plotted versus the ratio for the Namib, Bagnold sands. Gray shaded areas indicate oxides or elements where measured compositions are ±10% of the estimated Martian crust. Blue shaded areas along the diagonal line indicate compositions within ±10% of the composition of Namib, Bagnold sands. Computed, volatile-free compositions are used in Figures 19b and 19c.

and Gale craters differ by 15% relative for several major elements (Figure 14c). Data from Gale crater Bagnold sands and sandstones suggest that the sand-sized fraction in rocks and soils is not homogenized (Figure 19). Comparisons of sands and sandstones within Gale crater to an estimate of average Mars crust [*McLennan*, 2012]

Table 5. Average APXS Unit Data Used for the Compilation in Figure 19 With Bradbury Sandstone Rock Data (First Three Entries) Are From *Siebach et al.* [2017], and Estimated Mars Crust Is From *McLennan* [2012]

	SiO_2	Al_2O_3	TiO_2	FeO	MgO	CaO	Na_2O	K_2O	Cr_2O_3	MnO	Ni	Zn	P_2O_5	SO_3	Cl	Br
Group Average																
Bradbury_FineSandstone_Avg	41.27	7.36	0.98	22.86	9.59	5.93	2.03	1.86	0.52	0.53	346.35	2509.65	0.79	4.78	1.08	670.15
Bradbury_Sandstone_Avg	42.71	8.71	0.89	20.44	8.56	6.16	2.67	1.63	0.53	0.39	300.27	1077.23	0.76	5.16	1.14	234.18
Stimson_Avg	43.69	9.62	0.92	18.67	8.57	6.43	2.81	0.44	0.40	0.37	440.05	359.03	0.89	5.80	1.26	228.41
All_Gale_Fines_Avg	44.92	9.15	0.90	19.04	9.03	7.01	2.55	0.49	0.38	0.40	562.76	277.16	0.80	4.49	0.66	42.48
Bagnold_Avg	46.58	8.88	0.78	19.22	9.92	6.91	2.34	0.42	0.33	0.38	630.22	181.11	0.75	2.88	0.49	46.44
Estimated Mars crust (volatile free)	49.30	10.50	0.98	18.20	9.06	6.92	2.97	0.45	0.38	0.36	337.00	320.00	0.90			
Group Standard Deviation																
Bradbury_FineSandstone_StDev	1.98	1.28	0.15	2.41	1.84	0.77	0.96	1.17	0.18	0.12	100.71	1549.11	0.12	1.49	0.29	661.47
Bradbury_Sandstone_StDev	2.57	1.33	0.11	2.55	1.02	0.43	0.94	0.81	0.15	0.09	88.34	487.72	0.19	1.89	0.33	258.97
Stimson_StDev	2.58	1.38	0.05	2.28	1.17	0.59	0.21	0.07	0.08	0.07	88.13	140.12	0.18	2.62	0.42	131.98
All_Gale_Fines_StDev	1.85	0.80	0.16	1.60	1.33	0.28	0.37	0.12	0.10	0.04	137.56	124.45	0.20	1.63	0.19	25.47
Bagnold_StDev	1.18	0.92	0.07	1.37	1.69	0.37	0.36	0.06	0.07	0.03	160.63	44.56	0.04	0.36	0.06	25.92

indicate that many elements are within an ~10% range in compositional variation (Figure 19b). Yet it is also apparent that the specific differences are significant, related to the combined effects of physical sorting of sands, differences in source materials, and diagenesis of sedimentary rocks. This conclusion is similar to those from prior analyses of orbital data of dust-free regions [*Rogers and Hamilton*, 2015] and MER in situ spectroscopic data [*Ruff et al.*, 2014], which also show variation in mineral absorption features between locations with unconsolidated materials. Thus, the use of any average composition in compositional models to explain specific deposits should be performed with caution, though the overall basaltic character of Bagnold sands is confirmed. Further, more detailed modeling of the effects of size segregation and aeolian transport on composition, employing some of the data acquired here, could advance understanding of the regional and global differences in Martian soils.

5. Conclusions

All Curiosity rover instruments and capabilities for production of sieved size separates of samples were used in a campaign to study the composition and grain-scale characteristics of the Bagnold dune field. A full suite of measurements was collected at the Gobabeb site on the active Namib dune, and opportunistic measurements were obtained near High Dune. Grains studied at Gobabeb are well rounded to subrounded, typically range in size from very fine to medium sand (~50 to ~500 μm), and the size ranges are the same at the surface and within the upper ~20 cm. The sand patch near High dune is less homogenized and also has a fraction of reddish fine-grained (<50 μm) materials, which may be air fall dust due to less vigorous/frequent winds. The observed grain sizes in the Bagnold dunes are significantly darker, coarser, and better sorted than aeolian materials measured at Rocknest at Gale crater and elsewhere along the rover traverse. The bulk Bagnold dune sands also are better sorted and typically coarser than previous aeolian materials examined by the Spirit and Opportunity rovers. The differences between Namib dune and all prior soils measured are likely due to their activity, which removes silt- and clay-sized fractions.

Overall, active Martian dune sands are compositionally different from smaller Martian bedforms and typical soils. The basaltic mineralogy and lack of evidence for crystalline hydrous minerals in the Bagnold sands at Gobabeb are similar to that of the small Rocknest bedform but the chemistry exhibits several key differences. The active Namib sands are enriched in Mg, Si, and Ni and depleted in Na, Al, Zn, Ti, P, and Cr relative to other fines; this likely results from a higher abundance of olivine and pyroxene, lower abundances of sodium feldspars, and lower dust content. Grain size segregation is also apparent chemically with Si, Mg, and Ni enrichment in the 150 μm to 1 mm fraction relative to the <150 μm fraction and differences in release temperature profiles of CO_2, NO, and SO_2 volatiles between size fractions. All instruments show that the Gobabeb sands examined are depleted in H_2O, S, and Cl relative to other Martian soils and most rock targets examined by this and prior landed missions. But not all volatiles are depleted; CO_2 and NO are among the highest measured in Gale crater by SAM and are similar in abundance at Rocknest. In contrast to Rocknest, which had some low-temperature release of H_2O, implicating adsorbed water, the release temperatures for Gobabeb

samples are more consistent with hydroxylated phases or mineral bound water. Given the lack of crystalline volatile-bearing minerals, the differences in volatile content must be attributed to differences in the composition and/or proportion of XRD-amorphous phases. Collectively, the data indicate two distinct XRD-amorphous volatile reservoirs in Martian soils: (1) phases of mostly Si, Fe, and Al that are products of incipient aqueous alteration of silicates to form poorly crystalline hydroxylated phases, glasses with water inclusions, or both, and (2) phases enriched in Fe, Cl, S, and Zn that host a significant fraction of adsorbed water and exclusively reside in the <40 μm particle fraction. Within the Bagnold dunes, only amorphous phase (1) is present in appreciable amounts, while amorphous phase (2) dominates in finer-grained sands and soils like Rocknest and is consistent with nanophase iron oxides in dusts observed by MER.

Although the examined Bagnold dune sands are basaltic and broadly similar to Gale crater sandstones as well as to estimates of average Mars crust composition, all sand-sized materials show significant compositional variation, indicating the likely importance of local processes. Erosion of local Stimson formation sandstone units might contribute to the Bagnold dunes, but Bradbury sandstones are unlikely to be a large contributor, due to observed chemical differences. Comparison of the Gale crater sandstones to Bagnold sands highlights the role of syndepositional or diagenetic fluid-related processes in addition of Cl, S, and Br to the sandstones as well as changing the abundances of major cations and mafic minerals. Additional analyses of Martian sands and soils by Curiosity and in situ investigations on future missions will allow better attribution of which volatiles occur in dust, which reside in other fines, the precise carrier phases of volatiles, as well as the compositional effects of aeolian transport and sorting processes.

References

Achilles, C. A., et al. (2017), Mineralogy of an active eolian sediment from the Namib Dune, Gale Crater, Mars, *J. Geophys. Res. Planets*, *122*, doi:10.1002/2017JE005262.

Anderson, R. B., and J. F. Bell III (2010), Geologic mapping and characterization of Gale Crater and implications for its potential as a Mars Science Laboratory landing site, *Mars*, *5*, 76–128, doi:10.1555/mars.2010.0004.

Anderson, R. B., et al. (2015), ChemCam results from the Shaler outcrop in Gale crater, Mars, *Icarus*, *249*, 2–21.

Anderson, D. M., and A. R. Tice (1979), The analysis of water in the Martian regolith, *J. Mol. Evol.*, *14*, 33–38.

Anderson, R. C., et al. (2012), Collecting samples in Gale Crater, Mars: An overview of the Mars Science Laboratory Sample Acquisition, Sample Processing and Handling System, *Space Sci. Rev.*, doi:10.1007/s11214-012-9898-9.

Arvidson, R. E., et al. (2004a), Localization and physical properties experiments conducted by Spirit at Gusev Crater, *Science*, *305*, 821–824, doi:10.1126/science.1099922.

Arvidson, R. E., et al. (2004b), Localization and physical properties experiments conducted by Opportunity at Meridiani Planum, *Science*, *306*, 1730–1733, doi:10.1126/science.1104211.

Audouard, J., F. Poulet, M. Vincendon, R. E. Milliken, D. Jouglet, J.-P. Bibring, B. Gondet, and Y. Langevin (2014), Water in the Martian regolith from OMEGA/Mars Express, *J. Geophys. Res. Planets*, *119*, 1969–1989, doi:10.1002/2014JE004649.

Banham, S. G., S. Gupta, D. M. Rubin, J. A. Watkins, D. Y. Sumner, J. P. Grotzinger, K. W. Lewis, K. S. Edgett, L. A. Edgar, and K. M. Stack (2016), Reconstruction of an ancient eolian dune field at Gale Crater, Mars: Sedimentary analysis of the Stimson formation, *Proc. Lunar Planet. Sci. Conf. 47th*, 2346 pp., Houston, Tex.

Bandfield, J. L., K. S. Edgett, and P. R. Christensen (2002), Spectroscopic study of the Moses Lake dune field, Washington: Determination of compositional distributions and source lithologies, *J. Geophys. Res.*, *107*(E11), 5092, doi:10.1029/2000JE001469.

Banham, S. G., et al. (2017), The Stimson formation: Determining the morphology of a dry aeolian dune system and its climatic significance in Gale Crater, Mars, *Proc. Lunar Planet. Sci. Conf. 48th*, 2014 pp., Houston, Tex.

Bell, J. F., M. C. Malin, M. A. Caplinger, M. A. Ravine, A. S. Godber, M. C. Jungers, M. S. Rice, and R. B. Anderson (2012), Mastcam multispectral imaging on the Mars Science Laboratory rover: Wavelength coverage and imaging strategies at the Gale Crater field site, *Proc. Lunar Planet. Sci. Conf. 43rd*, 2541 pp.

Berger, J. A., et al. (2016), A global Mars dust composition refined by the Alpha-Particle X-ray Spectrometer in Gale Crater, *Geophys. Res. Lett.*, *43*, 67–75, doi:10.1002/2015GL066675.

Bibring, J.-P., et al. (1989), Results from the ISM experiment, *Nature*, *341*, 591–593.

Bish, D. L., et al. (2013), X-ray diffraction results from Mars Science Laboratory: Mineralogy of Rocknest at Gale Crater, *Science*, *341*(6153), 1238932, doi:10.1126/science.1238932.

Blake, D., et al. (2012), Characterization and calibration of the CheMin mineralogical instrument on Mars Science Laboratory, *Space Sci. Rev.*, *170*, 341–399, doi:10.1007/s11214-012-9905-1.

Blake, D. F., et al. (2013), Curiosity at Gale Crater, Mars: Characterization and analysis of the Rocknest sand shadow, *Science*, *341*, 1239505, doi:10.1126/science.1239505.

Bridges, N.T. and B.L. Ehlmann (2017), The Mars Science Laboratory (MSL) Bagnold Dunes campaign, Phase I: Overview and introduction to the special issue, *J. Geophys. Res. Planets*, *122*, doi:10.1002/2017JE005401.

Bridges, N. T., et al. (2012), Planet-wide sand motion on Mars, *Geology*, *40*(1), 31–34, doi:10.1130/G32373.1.

Bridges, N. T., et al. (2014), The rock abrasion record at Gale Crater: Mars Science Laboratory results from Bradbury Landing to Rocknest, *J. Geophys. Res. Planets*, *119*, 1374–1389, doi:10.1002/2013JE004579.

Bristow, T., et al. (2015), The origin and implications of clay minerals from Yellowknife Bay, Gale Crater, Mars, *Am. Mineral.*, *100*, 824–836, doi:10.2138/am-2015-5077CCBYNCND.

Buz, J., B. L. Ehlmann, L. Pan, and J. P. Grotzinger (2017), Mineralogy and stratigraphy of the Gale Crater rim, wall, and floor units, *J. Geophys. Res. Planets*, *122*, doi:10.1002/2016JE005163.

Cabrol, N. A., et al. (2008), Soil sedimentology at Gusev Crater from Columbia Memorial Station to Winter Haven, *J. Geophys. Res.*, *113*, E06S05, doi:10.1029/2007JE002953.

Cabrol, N. A., et al. (2014), Sands at Gusev Crater, Mars, *J. Geophys. Res. Planets*, *119*, 941–967, doi:10.1002/2013JE004535.

Campbell, J. L., et al. (2012), Calibration of the Mars Science Laboratory Alpha Particle X-ray Spectrometer, *Space Sci. Rev.*, *170*, 319–340, doi:10.1007/s11214-012-9873-5.

Clark, B. C., and A. K. Baird (1979), Volatiles in the Martian regolith, *Geophys. Res. Lett.*, *6*, 811–814, doi:10.1029/GL006i010p00811.

Cousin, A., et al. (2015), Compositions of sub-millimeter-size clasts and fine particles in the Martian soils at Gale: A window into the production of soils, *Icarus*, *249*, 22–42, doi:10.1016/j.icarus.2014.04/052.

Cousin, A., et al. (2017), Geochemistry of the Bagnold dune field as observed by ChemCam, and comparison with other aeolian deposits at Gale Crater, *J. Geophys. Res. Planets*, *122*, doi:10.1002/2017JE005261.

Day, M., and G. Kocurek (2016), Observations of an aeolian landscape: From surface to orbit in Gale Crater, *Icarus*, *280*, 37–71, doi:10.1016/j.icarus.2015.09.042.

Dehouck, E., S. M. McLennan, P.-Y. Meslin, and A. Cousin (2014), Constraints on abundance, composition, and nature of X-ray amorphous components of soils and rocks at Gale crater, Mars, *J. Geophys. Res. Planets*, *119*, 2640–2657, doi:10.1002/2014JE004716.

Edgar, L. A., et al. (2017), Shaler: In situ analysis of a fluvial sedimentary deposit on Mars, *Sedimentology*, doi:10.1111/sed.12370.

Edgett, K. S., and M. C. Malin (2000), New views of Mars eolian activity, materials, and surface properties: Three vignettes from the Mars Global Surveyor Mars Orbiter Camera, *J. Geophys. Res.*, *105*(E1), 1623–1650, doi:10.1029/1999JE001152.

Edgett, K. S., et al. (2012), Curiosity's Mars Hand Lens Imager (MAHLI) investigation, *Space Sci. Rev.*, *170*, 259–317, doi:10.1007/s11214-012-9910-4.

Edgett, K. S., et al. (2015), Curiosity's robotic arm-mounted Mars Hand Lens Imager (MAHLI): Characterization and calibration status, MSL MAHLI Tech. Rep. 0001 (Version 2: 05 October 2015), doi:10.13140/RG.2.1.3798.5447.

Edwards, C. S., et al. (2017), The thermophysical properties of the Bagnold Dunes, Mars: Ground-truthing orbital data, http://arxiv.org/abs/1711.10699.

Ehlmann, B. L., and J. Buz (2015), Mineralogy and fluvial history of the watersheds of Gale, Knobel, and Sharp craters: A regional context for the Mars Science Laboratory Curiosity's exploration, *Geophys. Res. Lett.*, *42*, 264–273, doi:10.1002/2014GL062553.

Ewing, R., et al. (2017), Sedimentary processes of the Bagnold Dunes: Implications for the eolian rock record of Mars, *J. Geophys. Res. Planets*, *122*, doi:10.1002/2017JE005324.

Feldman, W. C., et al. (2004), Global distribution of near-surface hydrogen on Mars, *J. Geophys. Res.*, *109*, E09006, doi:10.1029/2003JE002160.

Fraeman, A. A., B. L. Ehlmann, R. E. Arvidson, C. S. Edwards, J. P. Grotzinger, R. E. Milliken, D. P. Quinn, and M. S. Rice (2016), The stratigraphy and evolution of lower Mount Sharp from spectral, morphological, and thermophysical orbital data sets, *J. Geophys. Res. Planets*, *121*, 1713–1736, doi:10.1002/2016JE005095.

Gellert, R., et al. (2006), Alpha Particle X-ray Spectrometer (APXS): Results from Gusev crater and calibration report, *J. Geophys. Res.*, *111*, E02S05, doi:10.1029/2005JE002555.

Gellert, R., and B. C. Clark (2015), In-situ compositional measurements of rocks and soils with the Alpha Particle X-ray Spectrometer on NASA's Mars rovers, *Elements*, *11*, 39–44, doi:10.2113/gselements.11.1.39.

Goetz, W., et al. (2005), Indication of drier periods on Mars from the chemistry and mineralogy of atmospheric dust, *Nature*, *436*, 62–65.

Goetz, W., et al. (2010), Microscopy analysis of soils at the Phoenix landing site, Mars: Classification of soil particles and description of their optical and magnetic properties, *J. Geophys. Res.*, *115*, E00E22, doi:10.1029/2009JE003437.

Grant, J. A., S. A. Wilson, N. Mangold, F. Calef, and J. P. Grotzinger (2014), The timing of alluvial activity in Gale Crater, Mars, *Geophys. Res. Lett.*, *41*, 1142–1149, doi:10.1002/2013GL058909.

Gregory, H. E. (1950), Geology and geography of the Zion Park region, Utah and Arizona. A comprehensive report on a scenic and historic region of the southwest, *U.S. Geol. Surv. Prof. Pap., 220*, 200 pp. Washington, D. C.

Grotzinger, J. P., et al. (2014), A habitable fluvio-lacustrine environment at Yellowknife Bay, Gale Crater, Mars, *Science*, *343*, doi:10.1126/science.1242777.

Grotzinger, J., S. Gupta, M. Malin, D. Rubin, J. Schieber, K. Siebach, D. Sumner, K. Stack, A. Vasavada, and R. Arvidson (2015), Deposition, exhumation, and paleoclimate of an ancient lake deposit, Gale Crater, Mars, *Science*, *350*(6257), aac7575, doi:10.1126/science.aac7575.

Grotzinger, J. P., et al. (2005), Stratigraphy and sedimentology of a dry to wet eolian depositional system, Burns formation, Meridiani Planum, Mars, *Earth Planet. Sci. Lett.*, *240*, 11–72, doi:10.1016/j.epsl.2005.09.039.

Hamilton, V. E., H. Y. McSween Jr., and B. Hapke (2005), Mineralogy of Martian atmospheric dust inferred from thermal infrared spectra of aerosols, *J. Geophys. Res.*, *110*, E12006–1149, doi:10.1029/2005JE002501.

Herkenhoff, K. E., et al. (2003), Athena Microscopic Imager investigation, *J. Geophys. Res.*, *108*(E12), 8065, doi:10.1029/2003JE002076.

Hobbs, S. W., D. J. Paull, and M. C. Bourke (2010), Aeolian processes and dune morphology in Gale Crater, *Icarus*, *210*, 102–115.

Houck, J. R., J. B. Pollack, C. Sagan, D. Schaack, and J. A. Decker Jr. (1973), High altitude infrared spectroscopic evidence for bound water on Mars, *Icarus*, *18*, 470–480.

Jerolmack, D. J., D. Mohrig, J. P. Grotzinger, D. A. Fike, and W. A. Watters (2006), Spatial grain size sorting in eolian ripples and estimation of wind conditions on planetary surfaces: Application to Meridiani Planum, Mars, *J. Geophys. Res.*, *111*, E12S02, doi:10.1029/2005JE002544.

Johnson, J. R., et al. (2015), ChemCam passive reflectance spectroscopy of surface materials at the Curiosity landing site, Mars, *Icarus*, *249*, 74–92, doi:10.1016/j.icarus.2014.02.028.

Johnson, J. R., et al. (2017), Visible/near-infrared spectral diversity from in situ observations of the Bagnold Dune Field sands in Gale Crater, Mars, *J. Geophys. Res. Planets*, *122*, doi:10.1002/2016JE005187.

Jouglet, D., F. Poulet, R. E. Milliken, J. F. Mustard, J.-P. Bibring, Y. Langevin, B. Gondet, and C. Gomez (2007), Hydration state of the Martian surface as seen by Mars Express OMEGA: 1. Analysis of the 3 mm hydration feature, *J. Geophys. Res.*, *112*, E08S06, doi:10.1029/2006JE002846.

Knox, E. G. (1968), Lunar soil: An engineering term, *Science*, *161*, 1260, doi:10.1126/science.161.3847.1260.

Lane, M. D., and P. R. Christensen (2013), Determining basaltic composition of olivine dunes in Gale Crater, Mars, from orbit: Awaiting ground truth from Curiosity, *Geophys. Res. Lett.*, *40*, 3517–3521, doi:10.1002/grl.50621.

Lapotre, M. G. A., B. L. Ehlmann, S. E. Minson, R. E. Arvidson, F. Ayoub, A. A. Fraeman, R. C. Ewing, and N. T. Bridges (2017), Compositional variations in sands of the Bagnold Dunes, Gale Crater, Mars, from visible-shortwave infrared spectroscopy and comparison with ground truth from the Curiosity rover, *J. Geophys. Res. Planets*, *122*, doi:10.1002/2016JE005133.

Lapotre, M., et al. (2016), Large wind ripples on Mars: A record of atmospheric evolution, *Science*, *353*(6294), 55–58, doi:10.1126/science.aaf3206.

Leask, E. K. and B. L. Ehlmann (2016), Identifying and quantifying mineral abundance through VSWIR microimaging spectroscopy: A comparison to XRD and SEM, in IEEE Proc. of 8th Workshop on Hyperspectral Image and Signal Processing: Evolution in Remote Sens. (WHISPERS 2016), 5 pp., Los Angeles, Calif., 21-24 Aug.

Le Deit, L., E. Hauber, F. Fueten, M. Pondrelli, A. P. Rossi, and R. Jaumann (2013), Sequence of infilling events in Gale Crater, Mars: Results from morphology, stratigraphy, and mineralogy, *J. Geophys. Res. Planets*, *118*, 2439–2473, doi:10.1002/2012JE004322.

Le Deit, L., et al. (2016), The potassic sedimentary rocks in Gale Crater, Mars, as seen by ChemCam on board Curiosity, *J. Geophys. Res. Planets*, *121*, 784–804, doi:10.1002/2015JE004987.

Leshin, L. A., et al. (2013), Volatile, isotope, and organic analysis of Martian fines with the Mars Curiosity rover, *Science*, *341*(6153) 1238937.

Litvak, M. L., et al. (2016), Hydrogen and chlorine abundances in the Kimberley formation of Gale Crater measured by the DAN instrument on board the Mars Science Laboratory Curiosity rover, *J. Geophys. Res. Planets*, *121*, 836–845, doi:10.1002/2015JE004960.

Mahaffy, P. R., et al. (2012), The Sample Analysis at Mars investigation and instrument suite, *Space Sci. Rev.*, *170*, 401–478, doi:10.1007/s11214-012-9879-z.

Malin, M. C., and K. S. Edgett (2000), Sedimentary rocks of early Mars, *Science*, *290*, 1927–1937, doi:10.1126/science.290.5498.1927.

Malin, M. C., et al. (2017), The Mars Science Laboratory (MSL) mast cameras and descent imager: l. Investigation and instrument descriptions, *Earth Space Sci.*, doi:10.1002/2016EA000252.

Mangold, N., et al. (2016), Composition of conglomerates analyzed by the Curiosity rover: Implications for Gale Crater crust and sediment sources, *J. Geophys. Res. Planets*, *121*, 353–387, doi:10.1002/2015JE004977.

Maurice, S., et al. (2012), The ChemCam instrument suite on the Mars Science Laboratory (MSL) rover: Science objectives and mast unit description, *Space Sci. Rev.*, *170*, 95–166, doi:10.1007/s11214-012-9912-2.

Maurice, S., et al. (2016), ChemCam activities and discoveries during the nominal mission of Mars Science Laboratory in Gale crater, Mars, *J. Anal. At. Spectrom.*, *1*, 863–889, doi:10.1039/C5JA00417A.

McGlynn, I. O., C. M. Fedo, and H. Y. McSween Jr. (2011), Origin of basaltic soils at Gusev crater, Mars, by aeolian modification of impact-generated sediment, *J. Geophys. Res.*, *116*, E00F22, doi:10.1029/2010JE003712.

McLennan, S. M. (2012), Geochemistry of sedimentary processes on Mars, *SEPM Spec. Publ. No.*, *102*, 119–138.

McLennan, S. M., et al. (2014), Elemental geochemistry of sedimentary rocks at Yellowknife Bay, Gale Crater, Mars, *Science*, *343*, doi:10.1126/science.1244734.

McSween, H. Y., Jr., I. O. McGlynn, and A. D. Rogers (2010), Determining the modal mineralogy of Martian soils, *J. Geophys. Res.*, *115*, E00F12, doi:10.1029/2010JE003582.

Meslin, P.-Y., et al. (2013), Soil diversity and hydration as observed by Chemcam at Gale Crater, Mars, *Science*, *341*, doi:10.1126/science.1238670.

Milliken, R. E., J. F. Mustard, F. Poulet, D. Jouglet, J.-P. Bibring, B. Gondet, and Y. Langevin (2007), Hydration state of the Martian surface as seen by Mars Express OMEGA: 2. H_2O content of the surface, *J. Geophys. Res.*, *112*, E08S07, doi:10.1029/2006JE002853.

Milliken, R., R. C. Ewing, W. Fischer, and J. Hurowitz (2014), Wind-blown sandstones cemented by sulfate and clay minerals in Gale Crater, Mars, *Geophys. Res. Lett.*, *41*, 1149–1154, doi:10.1002/2013GL059097.

Milliken, R. E., J. P. Grotzinger, and B. J. Thomson (2010), Paleoclimate of Mars as captured by the stratigraphic record in Gale Crater, *Geophys. Res. Lett.*, *37*, L04201, doi:10.1029/2009GL041870.

Ming, D. W., et al. (2008), Geochemical properties of rocks and soils in Gusev Crater, Mars: Results of the Alpha Particle X-ray Spectrometer from Cumberland Ridge to Home Plate, *J. Geophys. Res.*, *113*, E12S39, doi:10.1029/2008JE003195.

Ming, D. W., et al. (2014), Volatile and Organic Compositions of Sedimentary Rocks in Yellowknife Bay, Gale Crater, Mars, *Science*, *343*, 1245267, doi:10.1126/science.1245267.

Minitti, M. E., et al. (2013), MAHLI at the Rocknest sand shadow: Science and science-enabling activities, *J. Geophys. Res. Planets*, *118*, 2338–2360, doi:10.1002/2013JE004426.

Mitrofanov, L. G., et al. (2012), Dynamic Albedo of Neutrons (DAN) experiment onboard NASA's Mars Science Laboratory, *Space Sci. Rev.*, *170*, 559–582, doi:10.1007/s11214-012-9924-y.

Mitrofanov, l. G., et al. (2014), Water and chlorine content in the Martian soil along the first 1900 m of the Curiosity rover traverse as estimated by the DAN instrument, *J. Geophys. Res. Planets*, *119*, 1579–1596, doi:10.1002/2013JE004553.

Morris, R. V., et al. (2006a), Mössbauer mineralogy of rock, soil, and dust at Gusev crater, Mars: Spirit's journey through weakly altered olivine basalt on the plains and pervasively altered basalt in the Columbia Hills, *J. Geophys. Res.*, *111*, E02S13, doi:10.1029/2005JE002584.

Morris, R. V., et al. (2006b), Mössbauer mineralogy of rock, soil, and dust at Meridiani Planum, Mars: Opportunity's journey across sulfate-rich outcrop, basaltic sand and dust, and hematite lag deposits, *J. Geophys. Res.*, *111*, E12S15, doi:10.1029/2006JE002791.

Morris, R. V., et al. (2016), Silicic volcanism on Mars evidenced by tridymite in high-SiO_2 sedimentary rock at Gale Crater, *Proc. Natl. Acad. Sci. U.S.A.*, *113*(26), 7071–7076, doi:10.1073/pnas.1607098113.

Morrison, S. M., et al. (2017a), Relationships between unit-cell parameters and compositions for rock-forming minerals on Earth, Mars, and other extraterrestrial bodies, *Am. Min.*, doi:10.2138/am-2018-6123.

Morrison, S. M., et al. (2017b), Crystal chemistry of Martian minerals from Bradbury landing through Naukluft Plateau, Gale Crater, *Am. Min.*, doi:10.2138/am-2018-6124.

Newman, C. E., et al. (2017), Winds measured by the Rover Environmental Monitoring Station (REMS) during the Mars Science Laboratory (MSL) rover's Bagnold Dunes Campaign and comparison with numerical modeling using MarsWRF, *Icarus*, *291*, 203–231, doi:10.1016/j.icarus.2016.12.016.

O'Connell-Cooper, C. D., et al. (2017), APXS-derived chemistry of the Bagnold dune sands: Comparisons with Gale Crater soils and the global Martian average, *J. Geophys. Res. Planets*, *122*, doi:10.1002/2017JE005268.

Pan, C., and A. D. Rogers (2017), Occurrence and scale of compositional heterogeneity in Martian dune fields: Toward understanding the effects of aeolian sorting on Martian sediment compositions, *Icarus*, *282*, 56–69.

Pelkey, S. M., B. M. Jakosky, and P. R. Christensen (2004), Surficial properties in Gale Crater, Mars, from Mars Odyssey THEMIS data, *Icarus*, *167*, 244–270, doi:10.1016/j.icarus.2003.09.013.

Petrone, A. (1970), The Moses Lake sand dunes, MS thesis, 89 pp., Wash. State Univ., Pullman.

Rogers, A. D., and P. R. Christensen (2007), Surface mineralogy of Martian low-albedo regions from MGS-TES data: Implications for upper crustal evolution and surface alteration, *J. Geophys. Res.*, *112*, E01003, doi:10.1029/2006JE002727.

Rogers, A. D., and O. Aharonson (2008), Mineralogical composition of sands in Meridiani Planum determined from Mars Exploration Rover data and comparison to orbital measurements, *J. Geophys. Res.*, *113*, E06S14, doi:10.1029/2007JE002995.

Rogers, A. D., and J. L. Bandfield (2009), Mineralogical characterization of Mars Science Laboratory candidate landing sites from THEMIS and TES data, *Icarus*, *203*, 437–453.

Rogers, A. D., and V. E. Hamilton (2015), Compositional provinces of Mars from statistical analyses of TES, GRS, OMEGA and CRISM data, *J. Geophys. Res. Planets*, *120*, 62–91, doi:10.1002/2014JE004690.

Ruff, S. W. (2004), Spectral evidence for zeolite in the dust on Mars, *Icarus*, *168*, 131–143.

Ruff, S. W., A. D. Rogers, V. E. Hamilton, and M. D. Kraft (2014), The misconception of a Mars global soil, in *Eighth International Conference on Mars*, 1461 pp., Pasadena, Calif.

Sanin A. B., et al. (2015), Data processing of the active neutron experiment DAN for a Martian regolith investigation, *Nuclear Inst. and Methods Phys. Res. Section A, 789*, 114–127.

Sautter, V., C. Fabre, O. Forni, M. Toplis, A. Cousin, A. Ollila, P. Meslin, S. Maurice, R. Wiens, and D. Baratoux (2014), Igneous mineralogy at Bradbury Rise: The first ChemCam campaign at Gale Crater, *J. Geophys. Res. Planets, 119*, 30–46, doi:10.1002/2013JE004472.

Schmidt, M. E., et al. (2014), Geochemical diversity in first rocks examined by the Curiosity Rover in Gale Crater: Evidence for and significance of an alkali and volatile-rich igneous source, *J. Geophys. Res. Planets, 119*, 64–81, doi:10.1002/2013JE004481.

Seelos, K. D., F. P. Seelos, C. E. Viviano-Beck, S. L. Murchie, R. E. Arvidson, B. L. Ehlmann, and A. A. Fraeman (2014), Mineralogy of the MSL Curiosity landing site in Gale Crater as observed by MRO/CRISM, *Geophys. Res. Lett., 41*, 4880–4887, doi:10.1002/2014GL060310.

Siebach, K. L., M. B. Baker, J. P. Grotzinger, S. M. McLennan, R. Gellert, L. Thompson, and J. A. Hurowitz (2017), Sorting out compositional trends in sedimentary rocks of the Bradbury group (Aeolus Palus), Gale Crater, Mars, *J. Geophys. Res. Planets, 122*, 295–328, doi:10.1002/2016JE005195.

Silvestro, S., D. A. Vaz, R. C. Ewing, A. P. Rossi, L. K. Fenton, T. I. Michaels, J. Flahaut, and P. E. Geissler (2013), Pervasive aeolian activity along rover Curiosity's traverse in Gale Crater, Mars, *Geology, 41*(4), 483–486, doi:10.1130/G34162.1.

Silvestro, S., D. A. Vaz, H. Yizhaq, and F. Esposito (2016), Dune-like dynamic of Martian aeolian large ripples, *Geophys. Res. Lett., 43*, 8384–8389, doi:10.1002/2016GL070014.

Smith, P. H., et al. (2009), Water at the Phoenix landing site, *Science, 325*, 58–61.

Soderblom, L. A., et al. (2004), Soils of Eagle Crater and Meridiani Planum at the Opportunity rover landing site, *Science, 306*, 1723–1726.

Stolper, E. M., et al. (2013), The petrochemistry of Jake_M: A Martian mugearite, *Science, 341*, doi:10.1126/science.1239463.

Sullivan, R., et al. (2005), Aeolian processes at the Mars Exploration Rover Meridiani Planum landing site, *Nature, 436*, 58–61, doi:10.1038/nature03641.

Sullivan, R., R. Arvidson, J. Bell, R. Gellert, M. Golombek, R. Greeley, K. Herkenhoff, J. Johnson, S. Thompson, and P. Whelley (2008), Wind-driven particle mobility on Mars: Insights from Mars Exploration Rover observations at El Dorado and surroundings at Gusev Crater, *J. Geophys. Res., 113*, E06S07, doi:10.1029/2008JE003101.

Sullivan, R., R. Anderson, J. Biesiadecki, T. Bond, and H. Stewart (2011), Cohesions, friction angles, and other physical properties of Martian regolith from MER wheel trenches and wheel scuffs, *J. Geophys. Res., 116*, E02006, doi:10.1029/2010JE003625.

Sullivan, R., B. Hallet, K. Herkenhoff, G. Kocurek, J. Kok, and the MSL Science Team (2014), Numerical modeling of wind-driven evolution of Martian fines, *Proc. Lunar Planet. Sci. Conf. 45th*, 1604 pp.

Sullivan, R. and J. Kok (2017), Aeolian saltation on Mars at low wind speeds, *J. Geophys. Res. Planets, 122*, doi:10.1002/2017JE005275.

Sutter, B., et al. (2017), Evolved gas analyses of sedimentary rocks and eolian sediment in Gale Crater, Mars: Results of the Curiosity Rover's Sample Analysis at Mars (SAM) instrument from Yellowknife Bay to the Namib Dune, *J. Geophys. Res. Planets, 122*, doi:10.1002/2016JE005225.

Tate, C. G., et al. (2015), Water equivalent hydrogen estimates from the first 200 sols of Curiosity's traverse (Bradbury Landing to Yellowknife Bay): Results from the Dynamic Albedo of Neutrons (DAN) passive mode experiment, *Icarus, 262*, 102–123.

Thomas, N., W. J. Markiewicz, R. M. Sablotny, M. W. Wuttke, H. U. Keller, J. R. Johnson, R. J. Reid, and P. H. Smith (1999), The color of the Martian sky and its influence on the illumination of the Martian surface, *J. Geophys. Res., 104*(E4), 8795–8808, doi:10.1029/98JE02556.

Thomson, B. J., N. T. Bridges, R. Milliken, A. Baldridge, S. J. Hook, J. K. Crowley, G. M. Marion, C. R. de Souza Filho, A. J. Brown, and C. M. Weitz (2011), Constraints on the origin and evolution of the layered mound in Gale Crater, Mars using Mars Reconnaissance Orbiter data, *Icarus, 214*(2), 413–432, doi:10.1016/j.icarus.2011.05.002.

Thompson, L. M., et al. (2016), Potassium-rich sandstones within the Gale impact crater. Mars: The APXS perspective, *J. Geophys. Res. Planets, 121*, 1981–2003, doi:10.1002/2016JE005055.

Tirsch, D., R. Jaumann, A. Pacifici, and F. Poulet (2011), Dark aeolian sediments in Martian craters: Composition and sources, *J. Geophys. Res., 116*, E03002, doi:10.1029/2009JE003562.

Treiman, A. H., et al. (2016), Mineralogy, provenance, and diagenesis of a potassic basaltic sandstone on Mars: CheMin X-ray diffraction of the Windjana sample (Kimberley area, Gale Crater), *J. Geophys. Res. Planets, 121*, 75–106, doi:10.1002/2015JE004932.

Vaniman, D., D. Bish, D. Ming, T. Bristow, R. Morris, D. Blake, S. Chipera, S. Morrison, A. Treiman, and E. Rampe (2014), Mineralogy of a mudstone at Yellowknife Bay, Gale Crater, Mars, *Science, 343*.

Wellington, D. F., et al. (2017), Visible to near-infrared MSL/Mastcam multispectral imaging: Initial results from select high-interest science targets within Gale Crater, Mars, *Am. Mineral.*, doi:10.2138/am-2017-5760CCBY.

Weitz, C. M., R. C. Anderson, J. F. Bell III, W. H. Farrand, K. E. Herkenhoff, J. R. Johnson, B. L. Jolliff, R. V. Morris, S. W. Squyres, and R. J. Sullivan (2006), Soil grain analyses at Meridiani Planum, Mars, *J. Geophys. Res., 111*, E12S04, doi:10.1029/2005JE002541.

Wiens, R. C., et al. (2012), The ChemCam instrument suite on the Mars Science Laboratory (MSL) Rover: Body unit and combined system tests, *Space Sci. Rev, 170*, doi:10.1007/s11214-012-9902-4.

Williams, R. M. E., et al. (2013), Martian fluvial conglomerates at Gale Crater, *Science, 340*, 1068–1072, doi:10.1126/science.1237317.

Yen, A. S., et al. (2005), An integrated view of the chemistry and mineralogy of Martian soils, *Nature, 436*, 49–54, doi:10.1038/nature03637.

Yen, A. S., et al. (2017), Multiple stages of aqueous alteration along fractures in mudstone and sandstone strata in Gale Crater, Mars, *Earth Planet. Sci. Lett., 471*, 186–198.